Elastic Tail Propulsion at Low Reynolds Number

by

Tony S. Yu

B.S. Mechanical Engineering
Columbia University, 2004

Submitted to the Department of Mechanical Engineering
in partial fulfillment of the requirements for the degree of

Master of Science in Mechanical Engineering

at the

MASSACHUSETTS INSTITUTE OF TECHNOLOGY

January 2007

Author . . . .
Department of Mechanical Engineering
January 19, 2007

Certified by . . . .
Anette E. Hosoi
Associate Professor, Mechanical Engineering
Thesis Supervisor

Accepted by . . . .
Lallit Anand
Chairman, Department Committee on Graduate Students

Elastic Tail Propulsion at Low Reynolds Number

by

Tony S. Yu

Submitted to the Department of Mechanical Engineering
on January 19, 2007, in partial fulfillment of the
requirements for the degree of
Master of Science in Mechanical Engineering

Abstract

A simple way to generate propulsion at low Reynolds number is to periodically oscillate a passive flexible filament. Here we present a macroscopic experimental investigation of such a propulsive mechanism. A robotic swimmer is constructed and both tail shape and propulsive force are measured. Filament characteristics and the actuation are varied and resulting data are quantitatively compared with existing linear and nonlinear theories.

Thesis Supervisor: Anette E. Hosoi
Title: Associate Professor, Mechanical Engineering

Acknowledgments

I would like to thank my advisor Anette “Peko” Hosoi; she has been an encouraging and supportive mentor since the day I first stumbled into her office. I hope in the future I will be able to balance teaching, research, and life as well as she does.

I could not have gotten through the tough times without the support and friendship of Sungyon Lee and Danielle Chou. Also, a special thanks to Eric Lauga for his advice on research and music.

Finally, love and thanks to my family, who have been supportive in all my ventures and to my lab mates, who have been like a second family to me.

Contents

List of Figures

List of Tables

Chapter 1

Introduction

Swimming at micro-scales has long been the realm of bacteria and other micro-organisms [3, 20], but recent advances in fabrication and manipulation at small scales have allowed researchers to catch up with nature [11]. At these small scales, the physics of swimming is fundamentally different than at human scales because the viscous forces of the fluid dominate inertial forces. Imagine falling into a swimming pool filled with honey; if we only considered inertial forces, it would seem that swimming in this pool should not be so different than swimming in a water-filled pool, because inertia is simply proportional to density and the density of honey is nearly the same as that of water. In reality, we expect it to be much harder to swim in honey because honey is "thicker"—or to be precise: more viscous—than water. Now if we return to a normal water-filled pool and shrink to the size of a bacterium, a funny thing occurs: this aqueous environment would appear to the bacteria much like that honey-filled pool. This similarity is determined by the Reynolds number of the flow. In this thesis, we focus on cases where the Reynolds number is small and hence viscous forces dominate.

1.1 Low Reynolds Number Swimming

The relative importance of inertial and viscous forces is reflected in the Reynolds number of the flow: $\mathrm{Re} = VL/\nu$, where ν is the kinematic viscosity of the fluid, V

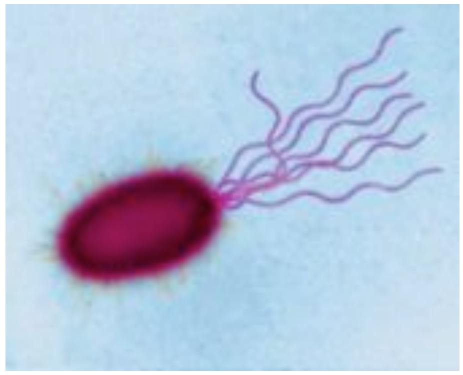

Figure 1-1: Transmission Electron Microscopy (TEM) image of *Escherichia coli* with multiple helical flagella from `http://www.astrographics.com/` – Dennis Kunkel.

is a characteristic velocity, and L is a characteristic length. If the Reynolds number is low (*i.e.* $\mathrm{Re} \ll 1$), viscous forces dominate inertial forces. In contrast to the honey-filled pool at the beginning of this chapter, low Reynolds number flows usually involve small scales and low velocities since many common fluids have relatively small kinematic viscosities ($\nu_{\mathrm{water}} \approx 10^{-6}$, $\nu_{\mathrm{air}} \approx 10^{-5}$)[1]. For example, consider a vertically-challenged human of one meter in height; he would need to move at a rate of less than $1\,\mu m/s$ in water to be considered a low Reynolds number swimmer! Thus, when we speak of "low Reynolds number swimming", we are generally referring to incredibly small swimmers, *i.e.* micro-organisms. For *E. coli*, with $L \approx 3\,\mu\mathrm{m}$ and $V \approx 30\,\mu\mathrm{m/s}$ [4], the Reynolds number is 10^{-4}; this can certainly be considered small and inertial forces are quite negligible. Low Reynolds number flow is also referred to as Stokes flow, creeping flow, or viscous flow and can have peculiar effects that are very different from those observed in our inertia-dominated world.

When viscous forces dominate, it is not simply "harder" to swim, as one might expect from the honey-filled pool analogy. To produce net translation in these conditions, the swimming motion must be both cyclic and non-reciprocal, as described by E.M. Purcell in his famous lecture, *Life at Low Reynolds Numbers* [26]. Much like the cyclic butterfly stroke of a human swimmer, any self-propelling motion should

[1] This is not always the case, of course—as exemplified by the unfortunate insects that get trapped in tree resin and become fossilized in amber.

be periodic if you want to generate continuous, net motion[2]. This requirement is especially true in Stokesian regimes because viscous forces quickly kill the velocity generated by a single stroke[3]. The second condition is required because a reciprocal motion leaves a swimmer oscillating in place, as shown by the "Scallop Theorem" (see [26] and §2.1).

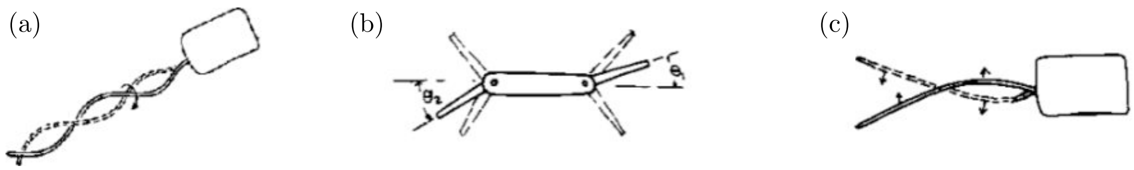

Figure 1-2: Sketches of theoretical swimmers from Purcell's *Life at Low Reynolds Numbers* [26]. (a) The corkscrew, (b) the three-link swimmer, and (c) the flexible-oar.

In his lecture, Purcell described three simple mechanisms that are not time-reversible and lead to swimming at these small scales; these swimmers are shown in Fig. 1-2: (a) the "corkscrew", (b) the "three-link swimmer", and (c) the "flexible oar"[4].

The corkscrew rotates a helical filament to generate propulsion and is analogous to the swimming mechanism of many bacteria, notably *E. coli* [2, 3]. In the early 1950s, G.I. Taylor investigated the physics of low Reynolds number swimming [32, 33] and described two methods of self-propulsion: sheets propagating waves of lateral displacement and cylindrical tails propagating helical waves, *i.e.* the corkscrew. In both models, the wave form was specified and the resulting hydrodynamic forces were used to calculate the propulsion generated. To test his corkscrew model, Taylor devised a clever swimmer using a wound elastic band to rotate a helical tail, as shown in Fig. 1-3. Since Taylor's time, many fluid mechanicians have studied various aspects of helical-tail swimmers[5]; for example: its efficiency [27], the effects of tail-flexibility [17, 37], the effects of nearby walls [19], and the bundling of multiple tails [15]. For a general overview of this swimmer, see Lighthill [20].

[2] If you were floating in a vacuum, free from any friction or air resistance, a single power stroke would carry you as far as you would want to go, but that is a bit impractical

[3] For example, a micron-sized swimmer moving at 30 μm/s in water would coast about 0.1 Å [26].

[4] It is interesting to note that all three mechanisms are essentially traveling waves.

[5] Of course, many biologists have studied them as well.

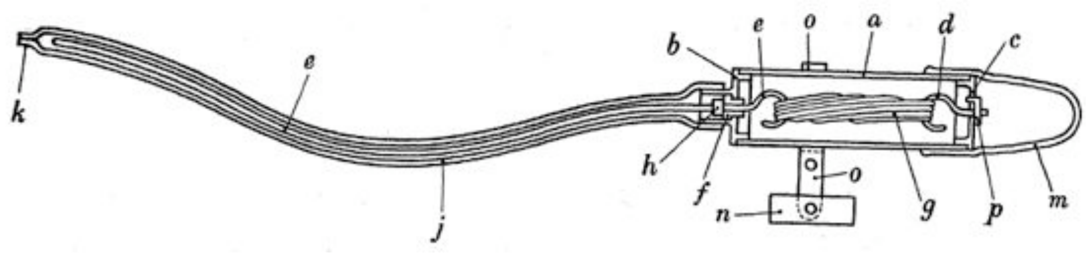

Figure 1-3: Diagram from [33] of G.I. Taylor's device to test his theory of waving cylindrical tails.

The three-link swimmer described by Purcell has three rigid links that move independently to produce a non-reciprocal motion. Becker, Koehler, and Stone [1] analyzed the motion of this swimmer and found an expression for the swimming velocity as a function of the angular amplitude between links. Chan and Hosoi [6] conducted experimental investigations of this swimmer, as shown in Fig. 1-4, that gave qualitative results similar to the developed theory. More recently, Tam and Hosoi [31] have investigated how the motion of the links can be coordinated to produce an "optimal" swimmer.

Figure 1-4: Experimental work by Chan and Hosoi on the motion of the three-link swimmer [6].

Purcell's final swimmer, the flexible oar, is the focus of this thesis. This swimmer has an elastic rod, or tail, that is free at one end and fixed to a body at the other end.

The fixed end of the tail oscillates, either transversely, angularly, or a combination thereof, generating travelling waves that produce a propulsive force. The shape of the tail is completely determined by a balance of elastic and hydrodynamic forces. Machin was the first to investigate this swimmer [23, 24] in hopes of determining whether this was the mechanism used by micro-organisms. After comparing the tail shapes generated by a waving elastic rod to those of microorganisms, Machin conjectured that known microorganisms had "active" tails, which could generate torques along the length of the tail. In more recent work, Wiggins & Goldstein [36, 35] developed a linear model describing the undulatory motion and propulsive force of a flexible tail driven by a transverse or angular oscillation at the fixed end. While this model was only valid for small deformations ($\mathrm{d}y/\,\mathrm{d}x \ll 1$, see Fig. 2-3), it closely resembled the motion of wiggling Actin filaments in experiments with large deformations. We note, however, that this comparison was qualitative and the propulsive force was not measured. Camalet & Jülicher [5] derived the nonlinear equations of motion for an elastic tail, allowing for active bending along the length of the tail. When solving the equations, however, they took the limit of small deformations to simplify calculations. Numerical simulations by Lowe [22] and Lagomarsino [18] described the motion of the tail without assuming small deformations and calculated the swimming speed of the flexible oar. A summary of work on elastic-tail swimmers is given in Tbl. 1.1.

Actuation	Experiment	Numerics	Linear Theory	Full Theory
Transverse Oscillation 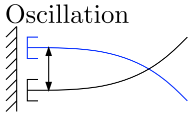	Wiggins, *et al.* [35]	Lowe [22] and Lagomarsino [18]	Wiggins, *et al.* [35] and Wiggins & Goldstein [36]	Camalet & Jülicher [5]
Angular Oscillation 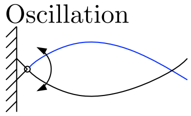	—	Lowe [22] and Lagomarsino [18]	Machin [23] and Wiggins & Goldstein [36]	Camalet & Jülicher [5]
Rotation 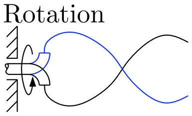	Koehler & Powers [17]	Lagomarsino [18]	—	Wolgemuth [37]

Table 1.1: Previous work on elastic-tail swimmers.

1.2 Motivation

As discussed in the last section, swimming at low Reynolds number usually refers to swimming at small scales. But why would one want to build such small swimmers? These micro-swimmers could provide propulsion for medical devices used for minimally invasive surgery or targeted drug delivery. Also, micro-swimmers could easily be adapted to work as a MEMS pump for "lab on a chip" applications. Kim *et al.* [16] (see Fig. 1-5) investigated such a pump, which used a mechanism very similar to the swimmer in this thesis.

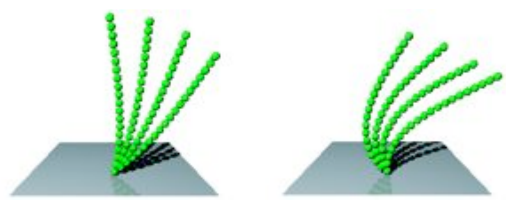

Figure 1-5: Simulation of pumping motion of angularly-oscillated filaments from Kim *et al.* [16]. This pump is analogous to the flexible oar fixed to a wall.

The swimmer we investigate, the flexible oar, could offer advantages over other Stokesian swimmers. Dreyfus, *et al.* have developed the first manmade micro-swimmers [11] (see also [28]) in which a chain of paramagnetic beads propagates a bending wave along the chain driven by an external magnetic field. This is essentially a multi-link swimmer, analogous to the three-link swimmer in §1.1, which requires multiple motors (torque-generating elements) along its tail. This complexity is avoided in the flexible oar, which requires a single motor at the tail's base; Purcell's other swimmer—the corkscrew—also uses a single motor. The difference between these motors is that the flexible oar employs an oscillatory forcing, while the corkscrew requires a continuous rotation. The later is quite easy to implement at large scales, while at micro-scales, the former *may* be simpler. These possible advantages have motivated our study of the flexible oar.

1.3 Thesis Summary

In this thesis, we investigate the angularly-actuated flexible oar design and test the validity of the linear model derived in Wiggins & Goldstein [36] comparing it to the waveforms and propulsive forces generated by a robotic, flexible-tail swimmer, dubbed "RoboChlam". For further comparison, we solve numerically the nonlinear equations presented in Camalet & Jülicher [5]. In the next chapter, we develop the nonlinear and linear equations of motion, from which we also derive an expression for the propulsive force. In Chapter 3, we describe the experiment used to test the theory and the Newton-Raphson method, which was used to solve the nonlinear equations. In Chapter 4, we present and discuss the results of our experiment. Finally, our conclusions and future work are presented in Chapter 5.

Chapter 2

Theory of Elastic Tail Swimming

Here we will present the theory behind the motion of an elastic tail at low Reynolds number. First, we review some key concepts of low Reynolds number flow, also known as Stokes flow, and then focus on the case of slender-bodies in this regime. Next we will solve for the elastic forces in the tail. The hydrodynamic and elastic forces are then balanced along the tail to find the equations of motion for the tail. From these equations, we derive a linear equation of motion and an expression for the propulsive force generated by a waving tail.

2.1 Stokes Flow and Reversibility

In general, the motion of a Newtonian fluid is governed by the Navier-Stokes equation:

$$\rho\frac{\partial \mathbf{u}}{\partial t} + \rho\mathbf{u}\cdot\nabla\mathbf{u} = \mu\nabla^2\mathbf{u} - \nabla p. \tag{2.1}$$

When the Reynolds number is low, the inertial terms in the above equation are negligible such that

$$-\nabla p + \mu\nabla^2\mathbf{u} = 0. \tag{2.2}$$

The above equation is known as the Stokes equation and states that, in the absence of external forces, pressure forces must balance viscous forces at all times. In addition, conservation of mass for an incompressible fluid requires a divergence free flow, such that

$$\nabla \cdot \mathbf{u} = 0. \tag{2.3}$$

By neglecting inertia, there exists a linear relationship between pressure forces and velocity, as given by the Stokes equation; this linearity means that the fluid flow is kinematically reversible, a property also known as time-reversibility (see [21, 7, 8]). The importance of this reversibility is discussed below.

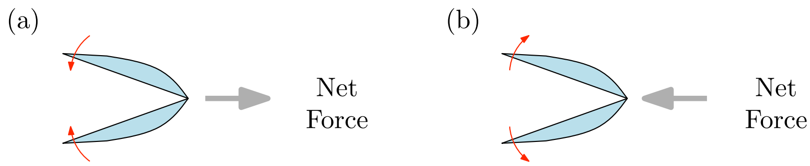

Figure 2-1: Schematic of hypothetical scallop at low Reynolds number. The net force generated during its closing motion (a) is equal and opposite to that generated during its opening motion (b).

In *Life at Low Reynolds Numbers* [26], E.M. Purcell described the consequences of kinematic reversibility on self-propelled swimmers using a hypothetical scallop as an example[1]. The scallop pictured in Fig. 2-1(a) closes the two halves of its shell and induces some velocity field $\mathbf{u}(x, y, z, t)$. This velocity field produces viscous stresses that must be balanced by pressure as given by the Stokes equation, and the resulting pressure adds up to produce a net force on the scallop. Because the fluid is kinematically reversible, a reversal of motion (Fig. 2-1b) produces an equal and opposite velocity field $-\mathbf{u}(x, y, z, t)$. Since the pressure is linearly related to the velocity, the opening stroke should produce a net force equal and opposite that of the closing stroke. This scallop would end up oscillating in place because it produces no *net* force over one cycle of motion. In fact, any low Reynolds number swimmer that changes its geometry through some deformation sequence and goes back to the original geometry using the reverse sequence will produce no net motion. This result is known as the "Scallop Theorem" and must be overcome for self-propulsion to occur.

[1] I call it hypothetical because scallops actually use jets of water for propulsion instead of the method described.

2.2 Slender Body Hydrodynamics

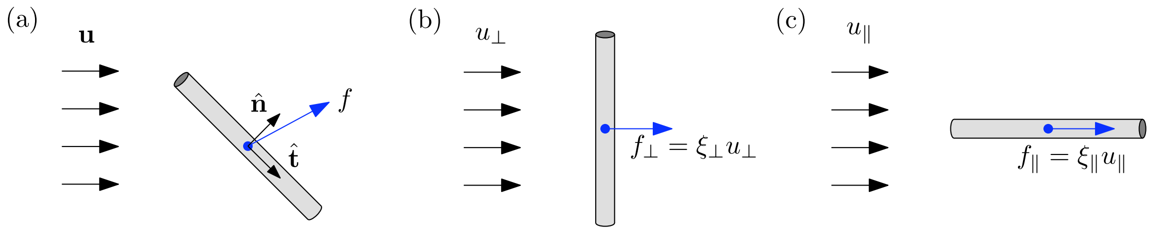

Figure 2-2: Slender cylinders in a low Reynolds number flow. The drag force per unit length, f, is linearly related to the velocity by drag coefficients $\xi_\perp$ and $\xi_\parallel$.

If the length of a body, L, is much greater than its diameter, D, ($L/D \gg 1$), Stokes equations can be further simplified using resistive force theory [4, 13, 20]. Applying this theory to a section of the tail, the drag force in Fig. 2-2(a) is broken down into components transverse and longitudinal to the tail axis (Fig. 2-2b and c, respectively). Thus, the drag forces on the tail are linearly related to the velocity by the transverse and axial drag coefficients, $\xi_\perp$ and $\xi_\parallel$. Since $u_\perp = \mathbf{u} \cdot \hat{\mathbf{n}}$ and $u_\parallel = \mathbf{u} \cdot \hat{\mathbf{t}}$, we see that

$$f_\perp = \xi_\perp \mathbf{u} \cdot \hat{\mathbf{n}}, \tag{2.4a}$$

$$f_\parallel = \xi_\parallel \mathbf{u} \cdot \hat{\mathbf{t}}. \tag{2.4b}$$

For a slender, cylindrical rod, these drag coefficients can be expressed as

$$\xi_\perp = \frac{4\pi\mu}{\ln\frac{L}{r} + 0.193} \tag{2.5a}$$

$$\xi_\parallel = \frac{2\pi\mu}{\ln\frac{L}{r} - 0.807} \tag{2.5b}$$

where μ is the viscosity of the fluid, and L and r are the length and radius of the rod. Eqs (2.5a) and (2.5b) are functions of the aspect ratio of the rod, defined as L/r, which by definition is quite large for a slender body. It is interesting to note that the drag coefficients, and consequently the drag force, are weak (logarithmic) functions of the tail radius.

To determine the drag force on the tail, we must now define a velocity. A point

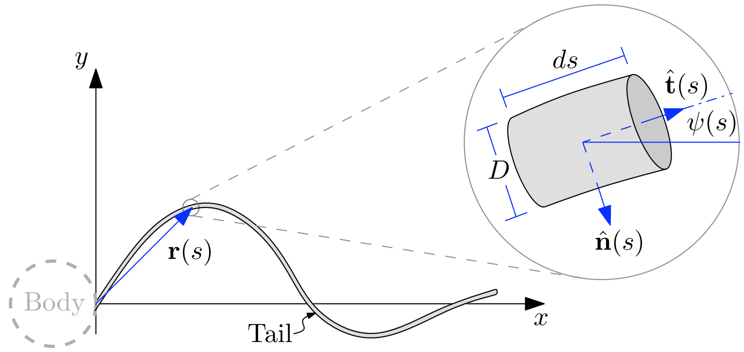

Figure 2-3: Elastic tail with tail base at the origin. The tail is parametrized by arclength s and has a tail shape given by the position vector $\mathbf{r}(s)$. Inset: tail element with length $\mathrm{d}s$, local angle ψ, unit normal $\hat{\mathbf{n}}$, unit tangent $\hat{\mathbf{t}}$. Additionally there is a local tension $\tau(s)$ acting on the cross section and defined positive outwards (not shown).

on the tail is defined by its position vector $\mathbf{r}$, as shown in Fig. 2-3, and has a velocity $\mathbf{r}_t$, where the subscript t denotes a time derivative. In a quiescent fluid, the *relative* velocity of the fluid would be $-\mathbf{r}_t$; thus, the total velocity is simply $\mathbf{u} - \mathbf{r}_t$, where $\mathbf{u}$ is the velocity of the fluid in the fixed frame. Now the drag force per unit length of the rod can be expressed as

$$\mathbf{f}_d = -[\xi_\perp \hat{\mathbf{n}}\hat{\mathbf{n}} + \xi_\| \hat{\mathbf{t}}\hat{\mathbf{t}}] \cdot (\mathbf{r}_t - \mathbf{u}), \tag{2.6}$$

where $\hat{\mathbf{n}}$ and $\hat{\mathbf{t}}$ are the unit normal and tangent to the filament, respectively. We consider a planar actuation of the rod, so that $\hat{\mathbf{n}}$ is defined without ambiguities to remain in this plane. Note that Eq. (2.6) is simply a vector expression for Eqs (2.4a) and (2.4b) with an additional transformation from the normal and tangent coordinates into a fixed coordinate system.

2.3 Elastic Forces

The elastic tail, with an arc length coordinate s, can be described by the position vector $\mathbf{r}(s)$, local angle $\psi(s)$, unit normal $\hat{\mathbf{n}}(s)$, and unit tangent $\hat{\mathbf{t}}(s)$, as shown in Fig. 2-3. The unit normal is described as "inward pointing" such that it points towards the center of curvature, and we consider a 2-D case where $\hat{\mathbf{n}}$ remains in the plane. The elastic forces on the rod are derived from an energy functional which includes its bending energy and its inextensibility constraint

$$\mathcal{E} = \int_0^L \left[\frac{A}{2}\kappa^2 + \frac{\Lambda}{2}\mathbf{r}_s{}^2 \right] \, \mathrm{d}s, \tag{2.7}$$

where the subscript s denotes a derivative, A is the bending stiffness, $\kappa \equiv \psi_s$ is the curvature of the tail, and Λ is the Lagrange multiplier enforcing inextensibility. Using calculus of variation we obtain the elastic force per unit length, $\mathbf{f}_\epsilon = -\delta\mathcal{E}/\delta\mathbf{r}$ as given by [5, 37]

$$\mathbf{f}_\epsilon = -(A\psi_{sss} - \psi_s\tau)\hat{\mathbf{n}} + (A\psi_{ss}\psi_s + \tau_s)\hat{\mathbf{t}}, \tag{2.8}$$

where $\tau = -\Lambda + A\kappa^2$ can be interpreted as the local tension in the tail. The details of this derivation are given in §B.1.

2.4 Nonlinear Equations

Camalet & Jülicher [5] derived the equations of motion for an elastic tail with torque generating elements along the tail. Here we have a passive tail with torque generated only at the base. Thus, the equations of motion for our swimmer are a simplified version of those derived in [5].

We have already found expressions for the only relevant forces in the system: the elastic forces in the tail and the drag forces from the fluid. We now enforce local mechanical equilibrium along the the tail, such that

$$\mathbf{f}_d + \mathbf{f}_\epsilon = 0. \tag{2.9}$$

Combining the above with Eqs (2.6) and (2.8), we find

$$\psi_t = -\frac{1}{\xi_\perp}\left(A\psi_{ssss} - \tau\psi_{ss} - \tau_s\psi_s\right) + \frac{1}{\xi_\parallel}\left(A\psi_s{}^2\psi_{ss} + \tau_s\psi_s\right), \tag{2.10a}$$

$$\tau_{ss} - \beta\tau\psi_s{}^2 = -A(1+\beta)(\psi_s\psi_{sss}) - A\psi_{ss}{}^2. \tag{2.10b}$$

The details of this derivation are given in §B.2. Eqs (2.10a) and (2.10b) are a pair of coupled nonlinear, partial differential equations that can be solved numerically.

2.5 Linear Equation

We can simplify Eqs (2.10a) and (2.10b) if we assume that the slope of the tail is small, *i.e.* $\psi \approx y_x \ll 1$ (subscript denotes derivative). This assumption leads to a linear, "hyperdiffusion" equation

$$y_t \approx -\frac{A}{\xi_\perp} y_{xxxx}, \tag{2.11}$$

as shown by Wiggins & Goldstein [36]. The details of this derivation are given in §B.3.

For the case of harmonic angular-actuation, we apply the boundary condition $\psi = a_0 \sin(\omega t)$ at the base (see next section). The nondimensionalization of Eq. (2.11) is obtained by substituting

$$x = L\tilde{x}, \qquad y = a_0 L\tilde{y}, \qquad t = \tilde{t}/\omega$$

into Eq. (2.11), leading to

$$\tilde{y}_{\tilde{t}} = -\frac{A/\omega\xi_\perp}{L^4}\tilde{y}_{\tilde{x}\tilde{x}\tilde{x}\tilde{x}} = -\left(\frac{\ell_\omega}{L}\right)^4 \tilde{y}_{\tilde{x}\tilde{x}\tilde{x}\tilde{x}}, \tag{2.12}$$

where $\ell_\omega = (A/\omega\xi_\perp)^{1/4}$ is the characteristic penetration length of the elastohydrodynamic problem; solutions to Eq. (2.11) decay exponentially in space over this typical length scale (see [35]). The time-evolution of the tail shapes is then only a function of the angular amplitude, a_0, and the dimensionless length,

$$\mathcal{L} = L/\ell_\omega = L\left(\frac{\omega\xi_\perp}{A}\right)^{1/4}. \tag{2.13}$$

This dimensionless length is the key parameter in the problem and represents the "floppiness" of the tail and hence the overall effectiveness of the swimmer. In particular, theory predicts an optimal dimensionless tail length as both short, stiff tails and long, flexible tails produce negligible net translation—the first is ineffective owing to the scallop theorem and the second owing to the excessive drag on the long passive filament.

Using separation of variables, the solution to Eq. (2.11) can now be found to be (see [35])

$$y(x,t) = a_0 \ell_\omega \Re\{e^{i\omega t} h(\eta)\}, \tag{2.14}$$

$$\text{where} \qquad \eta = \frac{x}{\ell_\omega} \qquad \text{and} \qquad h(\eta) = \sum_{j=1}^{4} c_j e^{i^j z_0 \eta}.$$

Here i is the imaginary number and the coefficients c_j must be solved using the boundary conditions of the problem, as discussed in the next section.

2.6 Boundary Conditions

In order to solve the equations of motion (Eqs 2.10a, 2.10b, and 2.11), we need to apply boundary conditions. On examination of Eqs (2.10a) and (2.10b), we find that there are four derivatives in the local angle, ψ, and two derivatives in the local tension, τ. As a result, we must supply four boundary conditions for ψ and two more for τ. For the linear equation, we have four derivatives in space and thus we supply four boundary conditions.

In this thesis, we investigate a "fixed" swimmer where one end of the tail is anchored and controlled in some manner; we call this the fixed end. The other end of the tail is free to move in the fluid; we call this the free end. To see how this applies to our equations of motion, let us revisit beam theory from undergraduate solid mechanics. Physically, we can interpret the variables of our equations as shown in Tbl. 2.1. Recall that subscripts denote derivatives and $A = EI$ is the bending stiffness, where E is the Young's modulus of the material and I is the cross-section moment of inertia. From beam theory, we know that the free end of the tail should be

Parameter	Linearized Equation	Nonlinear Equation
Displacement	y	$\int_0^s \psi \, \mathrm{d}s$
Slope/Angle	y_x	ψ
Moment	Ay_{xx}	$A\psi_s$
Transverse Force	Ay_{xxx}	$A\psi_{ss}$

Table 2.1: Physical interpretations of the tail shape and derivatives of the tail shape.

constrained to be forceless and torque-less. In the nonlinear equations, this translates to $\psi_{ss} = \psi_s = 0$, while in the linear equations, this translates into $y_{xxx} = y_{xx} = 0$. Finally, we must constrain the tension to be zero at the free end for the nonlinear case.

We intend to actuate the tail by prescribing the angle at the fixed end, which we will term the "base angle". Thus, the base angle is some function of time while the position at the fixed end is held constant. For the linear equations of motion, this is achieved by setting $y = 0$, to fix the position, and $y_x = f(t)$, to prescribe the base angle. For this thesis, we choose a harmonic oscillation, such that $y_x = a_0 \sin \omega t$. These boundary conditions are summarized in Tbl. 2.2.

Fixed End	Free End
$y = 0$	$y_{xx} = 0$
$y_x = a_0 \sin \omega t$	$y_{xxx} = 0$

Table 2.2: Boundary conditions on linear equations.

For the nonlinear equations, we prescribe the base angle by setting $\psi = a_0 \sin \omega t$, similar to our linear equations. Next, we balance the forces and torque at the base of the tail. In beam theory, this would be the same as solving for the reaction forces at the fixed end of a cantilever beam. To solve for the reaction forces, we imagine that there exists an identical tail attached to the base of the tail; this is depicted in Fig. 2-4. If this imaginary tail is antisymmetric to the real tail, then the forces exerted by the imaginary tail would exactly balance the forces exerted by the real tail. This imaginary tail implies that tension is equal on either side of the origin; mathematically, this is expressed by $\tau(0^-, t) = \tau(0^+, t)$. Similarly, the balance of forces transverse to the tail implies that $\psi_{ss}(0^-, t) = \psi_{ss}(0^+, t)$, because the force transverse to the tail is given by $A\psi_{ss}$, as shown in Tbl. 2.1.

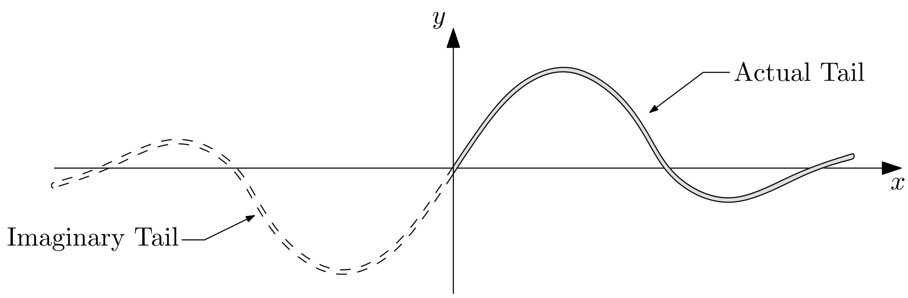

Figure 2-4: Elastic tail with antisymmetric, imaginary tail (dashed line) attached at the base. The imaginary tail produces forces equal and opposite that of the actual tail—this has the unfortunate consequence of producing a net torque at the base (origin).

There is one problem with the imaginary tail in Fig. 2-4: the net force produced adds to that of the real tail to produce a net torque about the origin. Thus, we do not have a simple relation to balance the torque and we must balance the torque generated by the drag forces along the tail with the torque applied at the base:

$$\sum M = \int_0^L \mathbf{r} \times f_d \, \mathrm{d}s + A\psi_s\Big|_{s=0} = 0, \tag{2.15}$$

where $\mathbf{r}$ is the position vector, f_d is the local drag force from Eq. (2.6), A is the bending stiffness, and ψ_s is the curvature. This equation gives a boundary condition on ψ_s. We could have made a similar calculation to balance the forces, of course, but the imaginary-tail idea is simpler to implement. Strangely, this torque boundary condition is the *fifth* boundary condition on ψ, instead of the four we predicted. This is because the angle, ψ, and the coordinate, s, do not describe absolute positions in space but instead, relative positions; the "extra" boundary condition fixes the position of the base in space. The boundary conditions on the nonlinear equations are summarized in Tbl. 2.3.

Fixed End	Free End
$\psi = a_0 \sin \omega t$	
$\psi_s = -\frac{1}{A}\int_0^L \mathbf{r} \times f_d \, \mathrm{d}s$	$\psi_s = 0$
$\psi_{ss}(0^-, t) = \psi_{ss}(0^+, t)$	$\psi_{ss} = 0$
$\tau(0^-, t) = \tau(0^+, t)$	$\tau = 0$

Table 2.3: Boundary conditions on coupled nonlinear equations.

2.7 Propulsive Force

The propulsive force is defined as the negative of the total hydrodynamic drag force in the direction of swimming [2]:

$$F \equiv -\int_0^L \mathbf{f} \cdot \hat{\mathbf{e}}_x \, \mathrm{d}s, \tag{2.16}$$

where $\mathbf{f}$ is the local force and $\hat{\mathbf{e}}_x$ is the unit vector in the direction of propulsion. Wiggins & Goldstein [36] derived the propulsive force by solving Eq. (2.16) using the local elastic force (2.8):

$$F = -\int_0^L \mathbf{f}_{\mathcal{E}} \cdot \hat{\mathbf{e}}_x \, \mathrm{d}s = -\hat{\mathbf{e}}_x \cdot \left[A\kappa_s \hat{\mathbf{n}} - A\kappa^2 \hat{\mathbf{t}} + \Lambda \hat{\mathbf{t}}\right]_0^L,$$
$$F \approx A(y_{xxx} - \frac{1}{2}{y_{xx}}^2)\big|_{x=0}. \tag{2.17}$$

Note, however, that this force equation does not depend on the difference in drag coefficients, $\xi_\perp$ and $\xi_\parallel$. But we expect a tail with isotropic drag ($\xi_\perp = \xi_\parallel$) to produce no net propulsion (see [1, 22]).

Our approach was to integrate the x-component of local drag force, Eq. (2.6), to yield the propulsive force

$$\langle F \rangle \approx -A\frac{\xi_\perp - \xi_\parallel}{\xi_\perp} \langle y_x y_{xxx} - \frac{1}{2} y_{xx}^2 \rangle_{x=0}, \tag{2.18}$$

where the small slope approximation was used and $\langle \ldots \rangle$ denotes averaging over one period of oscillation. The details of this solution are presented in §B.4. Note that

[2] Our swimmer moves from right to left (see Fig. 2-3), *i.e.* in the negative direction; thus, the negative sign in Eq. 2.16 defines the propulsive force to be positive from right to left.

Eq. (2.18) differs from Eq. (2.17) by a factor $(\xi_\perp - \xi_\parallel)/\xi_\perp$; this disparity arises from a proper integration of the drag force on the filament [22].

When comparing experiments to theory, it is useful to define a nondimensional propulsive force. Choosing the viscous penetration length, $\ell_\omega = (A/\omega\xi_\perp)^{\frac{1}{4}}$, as our characteristic length we find

$$x = \ell_\omega \tilde{x}, \qquad y = a_0 \ell_\omega \tilde{y}, \qquad t = T\tilde{t},$$

where a_0 is the angular amplitude, T is the period of oscillation, $\tilde{t}$ is the dimensionless time, and $\tilde{x}$ and $\tilde{y}$ are the nondimensional x and y, respectively. Substituting these dimensionless parameters into Eq. (2.18), we find[3]:

$$\begin{aligned}\langle F\rangle &= A\frac{\xi_\perp - \xi_\parallel}{\xi_\perp}\frac{1}{T}\frac{(a_0\ell_\omega)^2}{\ell_\omega^4}T\langle \tilde{y}_{\tilde{x}}\tilde{y}_{\tilde{x}\tilde{x}\tilde{x}} - \frac{1}{2}\tilde{y}_{\tilde{x}\tilde{x}}^2\rangle_{x=0} \\ &= (\xi_\perp - \xi_\parallel)|\omega| a_0^2\ell_\omega^2\langle \tilde{y}_{\tilde{x}}\tilde{y}_{\tilde{x}\tilde{x}\tilde{x}} - \frac{1}{2}\tilde{y}_{\tilde{x}\tilde{x}}^2\rangle_{x=0}, \\ &= a_0^2\ell_\omega^2(\xi_\perp - \xi_\parallel)|\omega|\langle\mathcal{F}\rangle. \end{aligned} \tag{2.19}$$

It follows that the nondimensional force is

$$\langle\mathcal{F}\rangle = \frac{\langle F\rangle}{a_0^2\ell_\omega^2(\xi_\perp - \xi_\parallel)|\omega|}. \tag{2.20}$$

The above equation is valid for all F even though it was derived using the linear expression for propulsive force.

[3] The $1/T$ comes from $\langle\ldots\rangle = \frac{1}{T}(\int_0^T \ldots \,\mathrm{d}t)$ and T comes from $\mathrm{d}t = T\,\mathrm{d}\tilde{t}$

Chapter 3

Methods and Implementation

To test the flexible oar theory presented in Chapter 2, we built a robotic swimmer; this swimmer is described in §3.1 followed by a description of the experimental setup. Section 3.3 describes how we measured the propulsive force generated by the swimmer. This is followed by a description of how tail shapes were captured and compared to theoretical tail shapes in §3.4. In §3.5, we describe the numerical solution of the nonlinear equations. Finally, we conclude with a short section dealing with the wall effects in our experiments.

3.1 Robotic Swimmer—"RoboChlam"

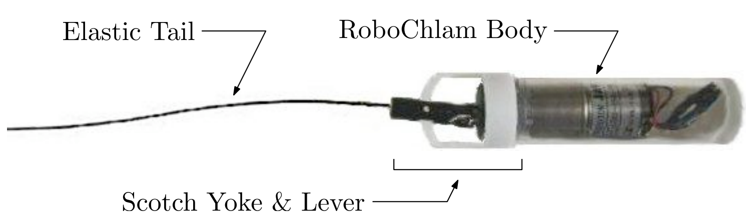

Figure 3-1: Robotic elastic-tail swimmer—dubbed "RoboChlam". The body houses a geared DC motor driven by an external power supply. The Scotch yoke and lever (see Fig. 3-2) convert the motor's rotation into an angular oscillation. A steel wire at the end of the lever acts as an elastic tail.

In order to experimentally quantify the propulsive characteristics of the "flexible oar" design, we built a robotic swimmer dubbed "RoboChlam" (after the algae

Chlamydomonas), as is displayed in Fig. 3-1. The RoboChlam body was approximately 8 cm in length and housed a Nidec Copal HG-16-240-AA geared DC motor. The motor's rotation was converted into an angular oscillation; consequently, the tail was angularly-actuated: the base of the filament was fixed at the origin and the base-angle was varied sinusoidally with an amplitude a_0 and a frequency ω. The voltage across the motor was supplied by a laboratory power supply and governed the oscillation frequency. The length of the lever, as shown in Fig. 3-2, controlled the amplitude of oscillation, and at the end of the lever, stainless steel wires of various lengths acted as elastic tails.

The rotation of the motor was converted to an angular oscillation using a combination of two mechanisms: a Scotch yoke and a lever. The Scotch yoke was made up of the rotor, rotor pin, and follower shown in Fig. 3-2(a). As the rotor rotates at a constant rate, the rotor pin traces out a circular motion. The pin moves the follower, which is constrained to remain vertical (see Fig. 3-2b). Since the follower is basically a vertical slot, whose width matches the diameter of the pin, the follower extracts the horizontal component of the pin's circular motion and "ignores" the vertical component. Thus, the horizontal position of the follower varied sinusoidally. The follower was connected to the lever by the follower pin, such that horizontal movement of the pin produced rotation of the lever about the pivot (see Fig. 3-2c). Thus, for a constant motor rotation rate, the mechanism produced an angular oscillation that was approximately sinusoidal[1].

3.2 Fixed Swimmer Experiment

RoboChlam was immersed in high viscosity silicone oil (polydimethylsiloxane, trimethylsiloxy terminated) to simulate the low Reynolds numbers experienced by microorganisms. A cantilever beam anchored RoboChlam (see Fig. 3-3), and a pair of

[1] Given the distance from the pivot to the follower pin L_0, the radius of the circle traced out by the rotor pin r_0, and the motor-rotation rate ω, the angle of the lever is expressed as $\alpha = \arcsin(\frac{r_0}{L_0}\sin\omega t)$, which is exactly sinusoidal when $r_0/L_0 \to 0$. Note, geometric constraints require $r_0/L_0 \leq 1$.

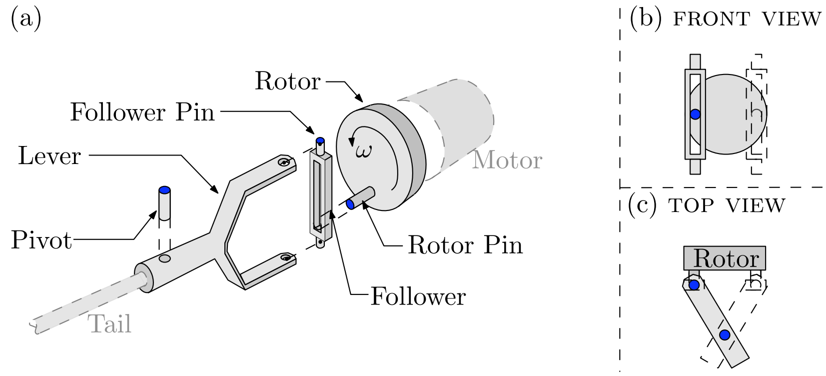

Figure 3-2: Scotch yoke and lever mechanism. The rotor and follower form the Scotch yoke, which converts the motor's rotation into a translational oscillation. A lever converts this translational oscillation into an angular oscillation.

strain gages on opposite sides of the beam measured beam deflection. Strain gage readings were converted into force measurements. A video camera captured video of the tail shapes generated by RoboChlam. Finally, videos of the tail shapes were digitized for comparison to our simulations and theoretical predictions.

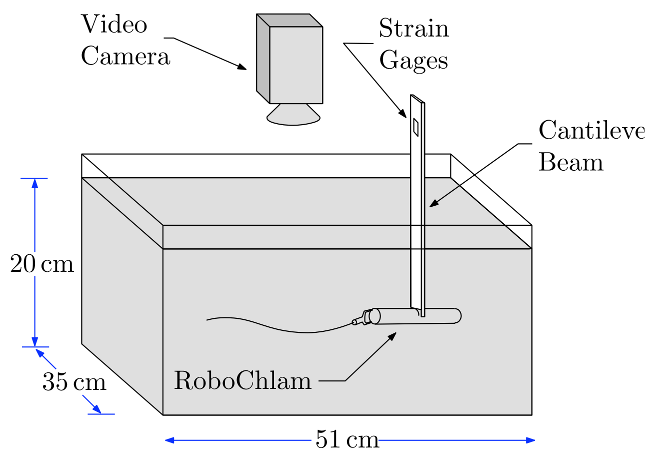

Figure 3-3: Schematic of experimental setup to measure tail shapes and the propulsive force of the elastic tail.

3.3 Propulsive Force Measurement

In order to measure the propulsive force of our swimmer, a cantilever beam with strain gages served as a force transducer. As shown, in Fig. 3-3, RoboChlam was mounted at the free end of the cantilever beam. The thrust generated by the swimmer exerted a force on the tip of the beam and deflected the beam. Strain gages mounted near the base of the cantilever beam measured the deflection as an electrical signal. The voltage output from the strain gages was processed using a Wheatstone bridge and two amplifiers. The resulting signal was then fed to a computer where the strain measurement was converted into a force measurement.

3.3.1 Beam Theory

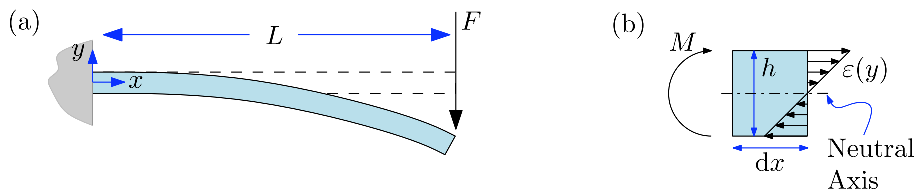

Figure 3-4: Diagram of cantilever beam. (a) Beam of length, L, thickness, h, and depth (into the page), b, with force, F applied at tip. (b) Free-body diagram of beam element of length dx with strain, $\epsilon(x, y)$, and moment, $M(x)$. Note that y is defined as zero at the neutral axis.

If a force is exerted at the tip of a cantilever beam of length L, thickness h, and width b, then the bending moment at an arbitrary point x is simply the product of the force and the moment arm:[2] $M = -F(L - x)$. From undergraduate solid mechanics, we can relate the moment to the stress with

$$\sigma = -\frac{My}{I}, \tag{3.1}$$

where, σ is the stress, y is the distance from the neutral axis, and $I = bh^3/12$ is the moment of inertia of the beam (see [9]). Using Hooke's law, $\sigma = E\varepsilon$, we relate the stress in the beam to the Young's modulus E and the strain ε. Putting these equations together we find that:

$$\varepsilon = \frac{F(L - x)y}{EI}. \tag{3.2}$$

In the above equation, we see that the strain of the beam is linearly proportional to

[2]Here, F has been defined positive downwards.

the force at the tip. Also note that the force at the tip can be amplified by using a long, thin beam and choosing a material with a low Young's modulus.

In our experiment, two strain gages were mounted at equal distances d from the base, but on opposite surfaces, $y = h/2$ and $y = -h/2$. As a result, the bending strain measured from these gages will be equal and opposite in sign.

3.3.2 Strain Gages

Strain gages are used to transform the strain in the cantilever beam into an electrical signal. Strain gages are essentially resistors that change resistance as they are stretched or compressed. The relationship between the resistance of the gages and the applied strain is given by

$$\frac{\mathrm{d}R}{R} = GF\varepsilon, \tag{3.3}$$

where GF is a constant of proportionality known as the gage factor, ε is the strain, and R is the nominal (undeformed) resistance of the strain gage (see [12]).

3.3.3 Wheatstone Bridge Circuit

To measure the change in resistance of the strain gages, we used a circuit known as a Wheatstone bridge (see Fig. 3-5). This bridge circuit is commonly used with strain gages, as they provide a means to zero the voltage and are ideal for temperature compensation. The relationship between the input voltage, V_{in}, and the output, $V_1 - V_2$, can be shown (see [12]) to be

$$V_1 - V_2 = V_{\mathrm{in}} \left[\frac{R_1 R_4 - R_2 R_3}{(R_1 + R_2)(R_3 + R_4)} \right] = V_{\mathrm{out},0}, \tag{3.4}$$

where we have defined $V_{\mathrm{out},0}$ to be the voltage output when there is no load on the beam, *i.e.* the strain gages are at their nominal resistances.

For the fixed swimmer experiment, the resistors R_2 and R_4 were chosen to equal the nominal resistances for the strain gages[3] R_1 and R_3 and from Eq. (3.4) we see

[3] In reality, R_4 was a potentiometer with variable resistance, but was very close to R_2 in resistance.

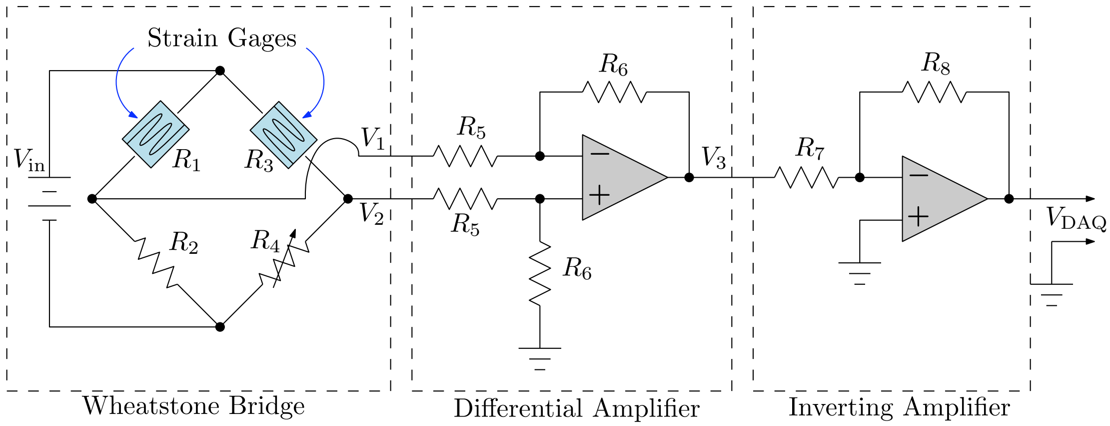

Figure 3-5: Diagram of circuit for strain gage measurement. The strain gages form two legs of the Wheatstone bridge whose output is amplified by two voltage amplifiers. The amplified signal is then sent to data acquisition equipment.

that the no-load voltage $V_{\text{out},0} = 0$. However, the resistances of the strain gages vary with beam deflection, so we take the derivative of Eq. (3.4) with respect to R_1 and R_3 to find

$$V_{\text{out}} = V_{\text{in}} \left[\frac{R_1 R_2}{(R_1 + R_2)^2} \left(\frac{\mathrm{d}R_1}{R_1} \right) + \frac{R_3 R_4}{(R_3 + R_4)^2} \left(-\frac{\mathrm{d}R_3}{R_3} \right) \right]. \tag{3.5}$$

Now recall from §3.3.1 that the strain on the strain gages is of equal and opposite magnitude so that $\mathrm{d}R_1 = -\mathrm{d}R_3 = \mathrm{d}R$ and define $R = R_1 = R_2 = R_3 = R_4$ so that Eq. (3.5) becomes

$$V_{\text{out}} = V_{\text{in}} \left[\frac{1}{4} \frac{\mathrm{d}R}{R} + \frac{1}{4} \frac{\mathrm{d}R}{R} \right] = V_{\text{in}} \frac{\mathrm{d}R}{2R}. \tag{3.6}$$

Thus the strain readings from the two gages sum and provide a slight amplification. Finally, we note that $\mathrm{d}R_1 = -\mathrm{d}R_3$ is only true for bending; for uniaxial tension or thermal expansion, $\mathrm{d}R_1 = \mathrm{d}R_3$ and from Eq. (3.5) we find there is no change in voltage output under these conditions.

3.3.4 Voltage Amplifiers

Although the force generated by the swimmer was modestly amplified by choosing a long cantilever beam and using two strain gages, further amplification was required. Because the output from the Wheatstone bridge, V_{out}, was actually a voltage difference, $V_1 - V_2$, the first amplification process used a differential amplifier, while the second used an inverting amplifier. For the differential amplifier in Fig. 3-5, it can be shown (see [12]) that

$$V_3 = \frac{R_6}{R_5}(V_1 - V_2) = \frac{R_6}{R_5}V_{\text{out}}. \tag{3.7}$$

Similarly an inverting amplifer produces an output

$$V_{\text{DAQ}} = -\frac{R_8}{R_7}V_3. \tag{3.8}$$

Now we can combine Eqs (3.2), (3.3), (3.6), (3.7), and (3.8) to find:

$$V_{\text{DAQ}} = -\frac{R_8}{R_7}\frac{R_6}{R_5}V_{\text{in}}\frac{GF}{2}\frac{F(L-d)\frac{h}{2}}{EI} = -V_{\text{in}}\frac{GF}{2}\frac{R_6R_8}{R_5R_7}\frac{(L-d)\frac{h}{2}}{EI}F, \tag{3.9}$$

recalling that the strain gages were positioned at $y_1 = h/2$, $y_2 = -h/2$, and $x_{1,2} = d$. Since we want to determine the propulsive force of our swimmer given an input voltage, we rearrange the above equation to find

$$F = -C_{NV}V_{\text{DAQ}}, \tag{3.10}$$

$$\text{where} \quad C_{NV} = \frac{2}{V_{\text{in}}GF}\frac{R_5R_7}{R_6R_8}\frac{EI}{(L-d)\frac{h}{2}}. \tag{3.11}$$

Thus, the conversion from Volts to Newtons is constant if the values on the right-hand side of Eq. (3.11) are constant.

3.3.5 Procedure for Force Measurement

A laboratory stand fixed one end of a thin beam made from DuPont™Delrin®. Omega®SG-6/120-LY13 strain gages were attached on opposite sides of the beam, equidistant from the fixed end. RoboChlam was then attached to the opposite end of the beam (free end), which held the swimmer in the silicone oil (see Fig. 3-3). The strain gages were attached to the strain gage circuit and the output from the circuit was attached to a National Instruments™BNC-2110 terminal block allowing the voltage output to be acquired by a personal computer. MATLAB®'s data acquisition toolbox was used to view the electrical signal produced by the strain gage circuit. The potentiometer on the Wheatstone bridge was adjusted until the voltage reading was nearly zero. Finally, RoboChlam was turned on for 2–10 periods of oscillation and the voltage at discrete increments of time (1/400 to 1/1500 s) was saved to file.

Tail Length L[m]	Tail Diameter D[mm]	Young's Modulus E[GPa]	Moment of Inertia I [m^4] $\times 10^{15}$	Bending Stiffness A [N $\cdot$ m^2] $\times 10^3$
0.18–0.3	0.51 & 0.61	190	3.3 & 6.8	0.62 & 1.3

Table 3.1: Tail parameters for fixed RoboChlam.

Fluid Viscosity μ[Pa $\cdot$ s]	Oscillation Frequency ω[rad/s]	Angular Amplitude a_0[rad]	Reynolds Number Re
3.18	0.4–5	0.814 & 0.435	10^{-2}–10^{-3}

Table 3.2: Experimental parameters for fixed RoboChlam.

Experiments showed that an angular oscillation starting with the tail at rest reached steady-state motion after approximately two periods of oscillation; this decay of transients was confirmed in our nonlinear simulations. Although force measurements required deflection of the cantilever beam, this deflection was less than half a centimeter at the beam's tip and thus, RoboChlam's position was approximately fixed. It was also observed that the oscillation of the tail produced an oscillatory torsion on the cantilever beam. Although a large beam width was chosen to reduce this effect, it was not completely eliminated. Since any prismatic (polygonal cross-section) beam under torsion will exhibit an axial strain [9], care had to be taken to eliminate this strain from our measurements. Thus, the configuration of the Wheatstone bridge and placement of strain gages were chosen to eliminate the effects of axial strain (see §3.3.3).

A sample trial of the raw voltage data is shown in Fig. A-1. Note that the raw data has zero-load readings at the beginning and end of the trial. This gave a quantitative measurement of the drift in the no-load voltage and was used as a measurement of

Young's Modulus E [GPa]	Beam Length L [m]	Beam Thickness h [cm]	Beam Width b [cm]	Moment of Inertia I [m^4]	Strain Gage Position d [cm]
3.1	0.26	0.297	1.88	4.1×10^{-11}	1.27

Table 3.3: Cantilever beam parameters.

error. From the raw data, a representative period was extracted taking care to avoid data near the no-load readings since these data are subject to transient effects in the tail motion. Since the desired result is the time-averaged propulsive force, the data over the representative period was averaged. The frequency of oscillation was also recorded from the voltage data by taking the inverse of the period. Finally, we note that a period of data consists of two intervals of positive propulsion (propulsive stroke) and two intervals of negative propulsion (recovery stroke), as shown in Fig. A-1, because of symmetry in the swimming motion.

Input Voltage V_{in} [V]	Gage Factor GF	Circuit Resistances (See Fig. 3-5) R [Ω]	R_5 [$k\Omega$]	R_6 [$k\Omega$]	R_7 [$k\Omega$]	R_8 [$k\Omega$]
5	2.13	120	10	500	10	1000

Table 3.4: Parameters for the strain gage circuit.

To convert these voltage readings to force, we had to first calibrate the force transducer. The gravitational force of a laboratory weight was applied to the tip of the cantilever beam. The beam was horizontally oriented for the calibration test so that the force of the calibration weight acted perpendicular to the beam, similar to what is shown in Fig. 3-4(a). Several trials were conducted with masses of 5, 10, and 20 kg. For each trial, the voltage from the strain gage circuit was measured before, during, and after application of the force; a sample calibration trial is given in Fig. A-2. The final voltage measurement was used to check for drift in the zero-load voltage. Averaging over the various trials produced a conversion factor $C_{NV} = 0.0159\,\frac{\text{N}}{\text{V}}$. We observed no statistically significant difference between the conversion factors produced by the three weights used; this result implies that the linear elastic approximation used in §3.3.1 was valid and viscoelastic effects of the plastic beam were negligible[4]. The time-averaged force was then found using Eq. (3.10). If we use the equation derived earlier for C_{NV} (Eq. 3.11) and the values from Tbls 3.3 and 3.4 instead of calibration measurements, we find $C_{NV} = 0.013\,\frac{\mathrm{N}}{\mathrm{V}}$. For all experimental data presented, the calibrated C_{NV} was used.

3.4 Tail Shape (Waveform) Comparison

A video camera was mounted perpendicular to the plane of motion of RoboChlam's tail, as shown in Fig. 3-6. The motion of the tail was recorded and the tail was digitized for comparison to theoretical results.

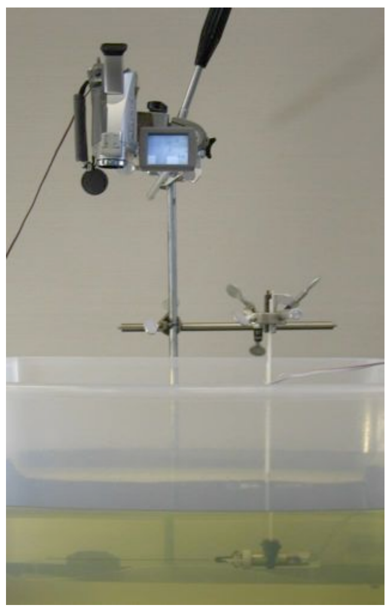

Figure 3-6: Photograph of experimental setup to measure tail shapes and propulsive force of elastic tail.

3.4.1 Video Acquisition

A Canon ZR65 MC digital video camcorder captured video of the tail shapes at 30 frames per second (fps) and 720 × 480 pixels per frame. The camera was connected

[4]The viscoelastic response is evident in Fig. A-2 as there is a slight rise in voltage during the application of force and a slight decline after release, but this effect is quite small.

by firewire to a personal computer running Windows XP, and WinDV was used to record video in DV-AVI type 2 format. The camera's focal plane was aligned with the tail's plane of motion, and the tail was centered in the frame. To eliminate transient effects, RoboChlam was turned on for a minimum of two periods of oscillation; after this time, a period of tail motion was recorded.

3.4.2 Image Processing

In order to compare the tail shapes captured on video to those predicted by theory, each video frame was processed using MATLAB®'s Image Processing Toolbox. Video of the experiment in DV-AVI format was read into MATLAB®[5] and converted into a sequence of grayscale images, like that in Fig. 3-7(a). The video was captured in interlaced format. To eliminate this distortion, every other horizontal line was removed from each image; every other vertical line was also removed to preserve scale, and the resulting resolution was 360 × 240 pixels per frame. These images were then converted to black and white images by setting dark pixels above a specified threshold to black and those below to white, as shown in Fig. 3-7(b).

Figure 3-7(c) shows the black and white image after a series of operations to filter the image and thin the tail to a line[6]. The image is then converted into data by storing the zero values (black pixels) as x-y coordinates according to their pixel locations. To set the origin of the data, the tail-shape data at successive time intervals was overlayed. The origin was then chosen at the pivot of the tail, as shown in Fig. 3-7(d). Finally, the data was scaled to units of meters and saved to file. A graphical user interface was built in MATLAB® to simplify this procedure (see Fig. A-3).

3.4.3 Comparing Experimental and Theoretical Tail Shapes

After videos of the tail shapes were digitized, they were compared to the theoretical tail shapes and the differences in shape were measured. To do this, the experimental

[5]MATLAB® had to be configured to read DV-AVI movies directly.

[6]The images were actually inverted, *i.e.* black and white pixels were flipped, because the filters in matlab treat black as the background and white as the foreground.

(a) Grayscale image from video.

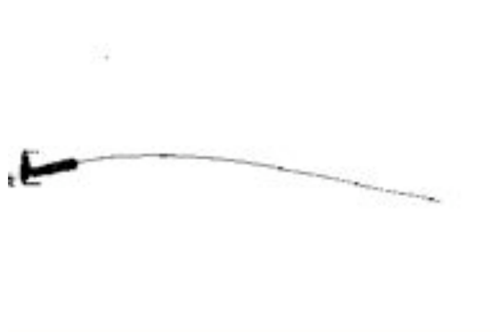

(b) Black and white image after thresholding grayscale image.

(c) Black and white image after filtering operations.

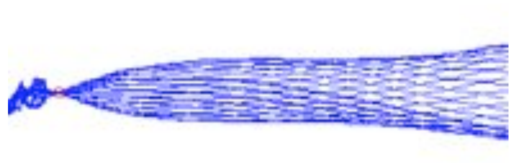

(d) Overlay of tail shape data at successive time intervals.

Figure 3-7: Processed images of tail shapes.

tail data had to be aligned and synchronized with those from the linear and nonlinear theories. A graphical user interface was built in MATLAB® to simplify this procedure (see Fig. A-4).

Video capture was synchronized with the tail motion by eye, so the tail position of the initial frame was unpredictable and had to be synchronized. Using the user interface, the digitized tail was plotted on top of the theoretical tails (linear and nonlinear). Slight adjustments were made in the digitized tail to account for offsets in the vertical position and rotational orientation. After that, the initial frame of the theoretical tails was adjusted to achieve the best alignment between the digitized tail and the theoretical ones. The linear and nonlinear tail equations were solved at time intervals equal to one fourth the time interval between video frames, *i.e.* 120 fps, to increase the accuracy of the alignment.

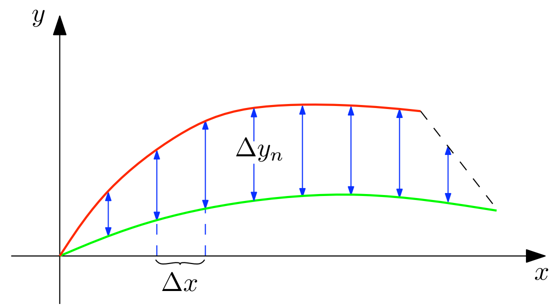

Figure 3-8: Schematic of two tails of different shapes. The difference in shape has been exaggerated for clarity. A line connects each tail-tip and the vertical distance Δy was measured at 100 equally spaced points along the tail.

To get a quantitative measurement of the difference between tails, we first found the difference in y-position between tails at 100 equally spaced points in the x-direction, where $\Delta x = L/100$ and L is the tail length. Note that the nonlinear and experimental tails extend to $x = L$ only when they are undeformed and exactly horizontal; on the other hand, the linear tail always extends to $x = L$ because of the small deformation approximation. To account for differences in length along x, a line is extended from the tip of the "shorter" tail to the tip of "longer" one before finding the tail differences, as shown in Fig. 3-8. Note that this idealized tip region contributed upwards of 10% of the difference measurement.

To complete this difference measurement, we use the Euclidean norm, given as

$$\|y\| = \sqrt{\sum_{n=1}^{100} {y_n}^2}. \tag{3.12}$$

For a nondimensional difference we divide this norm by the tail length and the number of points

$$\mathcal{D} = \frac{\|y\|}{100L}. \tag{3.13}$$

3.5 Numerical Solution of Nonlinear Equations

The nonlinear equations of motion (Eqs 2.10a and 2.10b) were solved numerically using a Newton-Raphson iteration, also known as Newton's method. What follows is a brief description of this method with an example of how it was applied to the nonlinear equations.

3.5.1 Newton's Method of Root-Finding

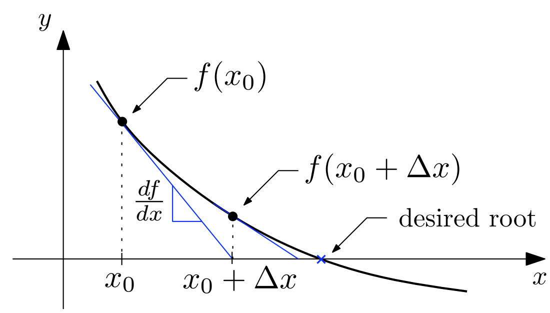

Figure 3-9: Arbitrary function, $f(x)$ near root. To find the root, we choose an initial point x_0 and find the slope $\mathrm{d}f/\mathrm{d}x$ at that point. By extending a line with slope $\mathrm{d}f/\mathrm{d}x$ to the x-axis, we march closer and closer to the root.

Suppose we are given some continuous function $f(x)$, which we can differentiate to give df/dx. Our goal is to find the point(s), x_r, where $f(x_r) = 0$; in other words, we want the root(s) of $f(x)$. We first choose an arbitrary point along the curve, x_0. Assuming $f(x)$ has a root and $f(x_0) \neq 0$ (otherwise, we need to look no further), there is some Δx for which

$$0 = f(x_r) \approx f(x_0 + \Delta x). \tag{3.14}$$

We can approximate Eq. (3.14) using the first two terms of the Taylor series expansion:

$$f(x_0) + \frac{df}{dx}\Big|_{x_0} \Delta x \approx 0$$

Solving for Δx, we have

$$\Delta x = \frac{-f(x_0)}{df/dx|_{x_0}}. \tag{3.15}$$

We can see from Fig. 3-9, that $f(x_0 + \Delta x) \neq 0$, but this new point is *closer* to zero[7]. We then iterate, to find the desired zero.

[7]It will not always be the case that $f(x_0 + \Delta x)$ is closer to zero than $f(x_0)$ – this has to do with the stability of this root-finding method (see Hamming [14]).

The algorithm is summarized below.

1. Given $f(x)$, find df/dx.
2. Choose a starting point x_0.
3. Calculate $\Delta x = \dfrac{-f(x_0)}{df/dx|_{x_0}}$.
4. Calculate $f(x_0 + \Delta x)$.
   - If this is close enough to zero, DONE.
   - Otherwise, let $x_0^{\text{new}} = x_0 + \Delta x$ and start over from step 3.

Of course, the definition of "close enough" to zero depends on the problem and the desired accuracy.

3.5.2 Finite Difference Equation

To demonstrate Newton's method of root-finding, we take a simplified form of Eq. (2.10a):[8] $\partial\psi/\partial t = -(A/\xi_\perp)\,\partial^4\psi/\partial s^4$. Before tackling this equation, we define $\phi \equiv \partial^2\psi/\partial s^2$ such that

$$\frac{\partial\psi}{\partial t} = -\frac{A}{\xi_\perp}\frac{\partial^2}{\partial s^2}\left(\frac{\partial^2\psi}{\partial s^2}\right) = -\frac{A}{\xi_\perp}\frac{\partial^2\phi}{\partial s^2}. \tag{3.16}$$

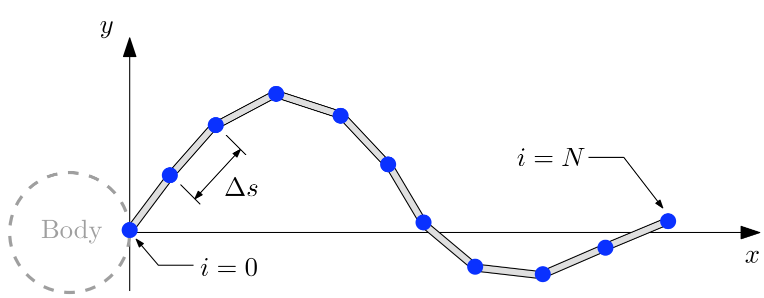

Figure 3-10: Discrete version of elastic tail. The tail is divided into N straight segments of length Δs. This allows derivatives to be approximated as difference equations.

As with most numerical schemes, we must replace the continuous problem with a discretized form. In Fig. 3-10, the smoothly-curving elastic tail (see Fig. 2-3) has

[8] Note, this simplified form is very similar to the linear equation of motion.

been replaced by N straight links of length Δs. What we have not shown is that time has also been divided into discrete time intervals, Δt. Next, we rewrite Eq. (3.16) in terms of finite differences at the nth time interval and the ith point along the tail:

$$\frac{\psi_i^{n+1} - \psi_i^n}{\Delta t} = -\frac{A}{\xi_\perp} \frac{\phi_{i+1}^{n+1} - 2\phi_i^{n+1} + \phi_{i-1}^{n+1}}{\Delta s^2}, \tag{3.17}$$

where subscripts denote the point (in space) along the tail and superscripts denote the increment in time. The left-hand side of Eq. (3.17) is the standard form for a backward, first difference in time; while the right-hand side is a centered, second difference in space[9]. The finite difference equation above is for the ith point along the tail at the nth time increment.

It is assumed that the nth variables are known and we are solving for the tail shape at the time, $n+1$. Note that we could have made all the superscripts on the right-hand side of Eq. (3.17) n instead of $n+1$; this is known as the explicit method since there would be a single unknown, ψ_i^{n+1}, on the left. The method we have chosen is termed "implicit" and was chosen for improved stability (see [25]).

Similarly the equation for ϕ is

$$\phi_i = \frac{\psi_{i+1} - 2\psi_i + \psi_{i-1}}{\Delta s^2}. \tag{3.18}$$

Here, it is implied that all the variables here are unknown and thus, are at time $n+1$; the superscript is left out for simplicity. Now we have a pair of equations to solve simultaneously—actually we must solve for this pair of equations at each point along the tail and thus, we have $2 \times N$ equations to solve simultaneously.

[9]Note: for the full equations, first derivatives in space appear and were approximated with forward differences.

3.5.3 Newton's Method in Multiple Dimensions

To make it clear how we are using Newton's method to solve these two finite difference equations, we move everything to the left-hand side:

$$f_1(\psi,\phi) = \frac{\psi_i^{n+1}-\psi_i^n}{\Delta t} + \frac{A}{\xi_\perp}\frac{\phi_{i+1}^{n+1}-2\phi_i^{n+1}+\phi_{i-1}^{n+1}}{\Delta s^2} = 0, \tag{3.19a}$$

$$f_2(\psi,\phi) = \phi_i - \frac{\psi_{i+1}-2\psi_i+\psi_{i-1}}{\Delta s^2} = 0. \tag{3.19b}$$

Now we are ready to solve our the nonlinear equations. First, we extend Eq. (3.14) to multiple dimensions (*i.e.*, multiple variables) and substitute f_1 and f_2 (Eqs 3.19a and 3.19b) for f to find:

$$\begin{aligned} f_1 &+ \frac{\partial f_1}{\partial \psi_{i-1}}\Delta\psi_{i-1} + \frac{\partial f_1}{\partial \psi_i}\Delta\psi_i + \frac{\partial f_1}{\partial \psi_{i+1}}\Delta\psi_{i+1} \\ &+ \frac{\partial f_1}{\partial \phi_{i-1}}\Delta\phi_{i-1} + \frac{\partial f_1}{\partial \phi_i}\Delta\phi_i + \frac{\partial f_1}{\partial \phi_{i+1}}\Delta\phi_{i+1} = 0, \end{aligned} \tag{3.20}$$

$$\begin{aligned} f_2 &+ \frac{\partial f_2}{\partial \psi_{i-1}}\Delta\psi_{i-1} + \frac{\partial f_2}{\partial \psi_i}\Delta\psi_i + \frac{\partial f_2}{\partial \psi_{i+1}}\Delta\psi_{i+1} \\ &+ \frac{\partial f_2}{\partial \phi_{i-1}}\Delta\phi_{i-1} + \frac{\partial f_2}{\partial \phi_i}\Delta\phi_i + \frac{\partial f_2}{\partial \phi_{i+1}}\Delta\phi_{i+1} = 0. \end{aligned} \tag{3.21}$$

The derivatives in the above equation are given in Tbl. 3.5. Here we have to solve for many zeros simultaneously; this problem naturally leads to a matrix representation of our equations.

$$\underbrace{\begin{bmatrix} f_{1,1} \\ f_{2,1} \\ \vdots \\ f_{1,N} \\ f_{2,N} \end{bmatrix}}_{\mathbf{f}} + \underbrace{\begin{bmatrix} \frac{\partial f_{1,1}}{\partial \psi_1} & \frac{\partial f_{1,1}}{\partial \phi_1} & \cdots & \frac{\partial f_{1,1}}{\partial \psi_N} & \frac{\partial f_{1,1}}{\partial \phi_N} \\ \frac{\partial f_{2,1}}{\partial \psi_1} & \frac{\partial f_{2,1}}{\partial \phi_1} & \cdots & \frac{\partial f_{2,1}}{\partial \psi_N} & \frac{\partial f_{2,1}}{\partial \phi_N} \\ \vdots & \vdots & \ddots & \vdots & \vdots \\ \frac{\partial f_{1,N}}{\partial \psi_1} & \frac{\partial f_{1,N}}{\partial \phi_1} & \cdots & \frac{\partial f_{1,N}}{\partial \psi_N} & \frac{\partial f_{1,N}}{\partial \phi_N} \\ \frac{\partial f_{2,N}}{\partial \psi_1} & \frac{\partial f_{2,N}}{\partial \phi_1} & \cdots & \frac{\partial f_{2,N}}{\partial \psi_N} & \frac{\partial f_{2,N}}{\partial \phi_N} \end{bmatrix}}_{\mathbf{J}} \underbrace{\begin{bmatrix} \Delta\psi_1 \\ \Delta\phi_1 \\ \vdots \\ \Delta\psi_N \\ \Delta\phi_N \end{bmatrix}}_{\Delta\mathbf{x}} = \begin{bmatrix} 0 \\ 0 \\ \vdots \\ 0 \\ 0 \end{bmatrix}. \tag{3.22}$$

Here, $\mathbf{J}$ is the matrix of first-order, partial derivatives, known as the Jacobian matrix. A second subscript has been added to each f to denote the value of i. Solving

Eq. (3.22) for $\Delta\mathbf{x}$, we find

$$\Delta\mathbf{x} = -\mathbf{J}^{-1}\mathbf{f}. \tag{3.23}$$

We then calculate $\mathbf{f}(\mathbf{x} + \Delta\mathbf{x})$ and see if the result is close enough to the zero vector. If not, we iterate to find the roots of our equations as outlined in §3.5.1. It is not reasonable, nor efficient (nor necessary), to seek the value of $\mathbf{x}$ that is precisely zero. Instead, we seek a solution whose error, which is generally called the residual, is below some threshold value. We take advantage of the fact that $\Delta\mathbf{x}$ approaches zero quadratically as we get closer to the solution. Thus, the residual was calculated as the maximum value of $|\Delta\mathbf{x}|$ to ensure the maximum error was below a threshold.

	$\partial/\partial\psi_{i-1}$	$\partial/\partial\psi_i$	$\partial/\partial\psi_{i+1}$	$\partial/\partial\phi_{i-1}$	$\partial/\partial\phi_i$	$\partial/\partial\phi_{i+1}$
f_1	0	$\dfrac{1}{\Delta t}$	0	$\dfrac{A}{\xi_\perp \Delta s^2}$	$\dfrac{-2A}{\xi_\perp \Delta s^2}$	$\dfrac{A}{\xi_\perp \Delta s^2}$
f_2	$\dfrac{-1}{\Delta s^2}$	$\dfrac{2}{\Delta s^2}$	$\dfrac{-1}{\Delta s^2}$	0	1	0

Table 3.5: Derivatives of finite differences.

Although this section only deals with a very simplified form of our equations of motion, it is a simple matter to replace Eqs (3.19a) and (3.19b) with Eqs (B.12a), (B.12b), and (B.12c) and solve for the $3 \times N$ variables, ψ_i, ϕ_i, and τ_i, along the tail with the boundary conditions given in Tbl. 2.3. The difference equations and their derivatives used in the numerical solution are given in Tbl. A.1.

3.6 Wall Effects

As shown in Fig. 3-3, RoboChlam is confined in a container with dimensions similar (of the same order of magnitude) to the tail length. Because of this proximity, special consideration must be given to the effect of the walls. Just as the force required to pull a plate in Couette flow is dependent on the gap distance, the drag on the tail depends on the distance to the walls. In fact, Vogel [34] states that "at a Reynolds number of 10^{-4}, the presence of a wall 500 diameters away from a cylinder doubles the effective drag." This wall effect was accounted for by the drag coefficients used.

The drag coefficients given in Eqs (2.5a) and (2.5b) are derived for a slender cylinder in an infinite, unbounded fluid. There exists a wealth of drag-coefficient equations to account for wall effects (compilations of these coefficients are given in [4, 30]). In choosing the drag coefficients for this experiment, we used the experimental results of Stalnaker and Hussey [30] that found best agreement with the drag coefficients from de Mestre and Russel [10]. We present them here without derivation:

$$\xi_\perp = \int_{-l}^{+l} \frac{-8\pi\mu\varepsilon}{2+\varepsilon\{\ln(1-x^2/l^2)+1-E_\perp\}} + \mathcal{O}(\varepsilon^3)dx, \tag{3.24}$$

$$\xi_\parallel = \int_{-l}^{+l} \frac{8\pi\mu\varepsilon}{4+\varepsilon\{2\ln(1-x^2/l^2)-2-E_\parallel\}} + \mathcal{O}(\varepsilon^3)dx, \tag{3.25}$$

where

$$\begin{aligned} E_\perp =& \operatorname{arcsinh}\left(\frac{1+x}{2d}\right) + \operatorname{arcsinh}\left(\frac{l-x}{2d}\right) + \frac{2(l+x)}{\{(l+x)^2+4d^2\}^{1/2}} \\ &+ \frac{2(l-x)}{\{(l-x)^2+4d^2\}^{1/2}} - \frac{(l+x)^3}{2\{(l+x)^2+4d^2\}^{3/2}} - \frac{(l-x)^3}{2\{(l-x)^2+4d^2\}^{3/2}} \end{aligned}$$

and

$$\begin{aligned} E_\parallel =& 2\operatorname{arcsinh}\left(\frac{1+x}{2d}\right) + 2\operatorname{arcsinh}\left(\frac{l-x}{2d}\right) + \frac{(l+x)}{\{(l+x)^2+4d^2\}^{1/2}} \\ &+ \frac{(l-x)}{\{(l-x)^2+4d^2\}^{1/2}} - \frac{2(l+x)^3}{\{(l+x)^2+4d^2\}^{3/2}} - \frac{2(l-x)^3}{\{(l-x)^2+4d^2\}^{3/2}}. \end{aligned}$$

As shown in Fig. 3-11, the length of the cylinder is $2l$, the distance to the wall d, and the radius of the cylinder r. These drag coefficients depend logarithmically on the aspect ratio of the rod as given by $\varepsilon = 1/\ln(2l/r)$. We do not take the limiting cases presented in [10] because d/l is order 1. Note that there are five wall in this experiment: fore, aft, below, and one on each side of the swimmer (see Fig. 3-3). For simplicity, we will only account for the effects of a single side wall, which is the dominant effect[10]. The effect of the back wall (aft of the swimmer) will vary and, at

[10]The bottom wall has a smaller effect on drag.

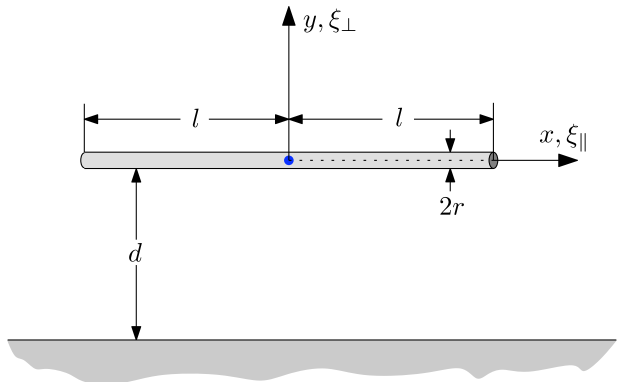

Figure 3-11: Schematic of slender rod of length $2l$ and a distance d from the wall.

times, dominates because we are using tails of different length so that the distance to the back wall varies. For our experiments, the distance to the side wall d is taken to be constant for simplicity, although this distance varies as the tail oscillates.

Chapter 4

Results and Discussion

The results of our investigations are summarized in Figs 4-1, 4-2 and 4-3. We first display in Fig. 4-1 the propulsive force generated for a range of dimensionless tail lengths, $\mathcal{L}$. All parameters of the experiment were known or measured, and no fitting of data was necessary. Figure 4-2 shows a comparison of the linear, nonlinear, and experimental tail shapes while Fig. 4-3 gives a quantitative measurement of the difference in tail shapes as a function of nondimensional length.

4.1 Propulsive Force

As shown in Fig. 4-1, agreement of the propulsive force with the theoretical (linear model, Eq. 2.11) and numerical values (nonlinear model, Eqs. 2.10a and 2.10b) is excellent. The force data from the RoboChlam experiments show a maximum dimensionless force at $\mathcal{L} = 2.14$, in agreement with prediction from the theory. Note that our data was nondimensionalized with the drag difference, $\xi_\perp - \xi_\parallel$ (see Eq. 2.20), instead of the transverse drag $\xi_\perp$, which was used in [36, 35]. The drag difference originated in Eq. (2.18), and it represents the correct scaling as a tail with isotropic drag ($\xi_\perp = \xi_\parallel$) should produce zero propulsive force [1, 22]. We note also that the maximum value of $\mathcal{L}$ that could be tested was limited by the motor's rotation rate and the length of tail that would fit in the experimental apparatus.

In comparing the data to linear elastohydrodynamic theories, there are three pri-

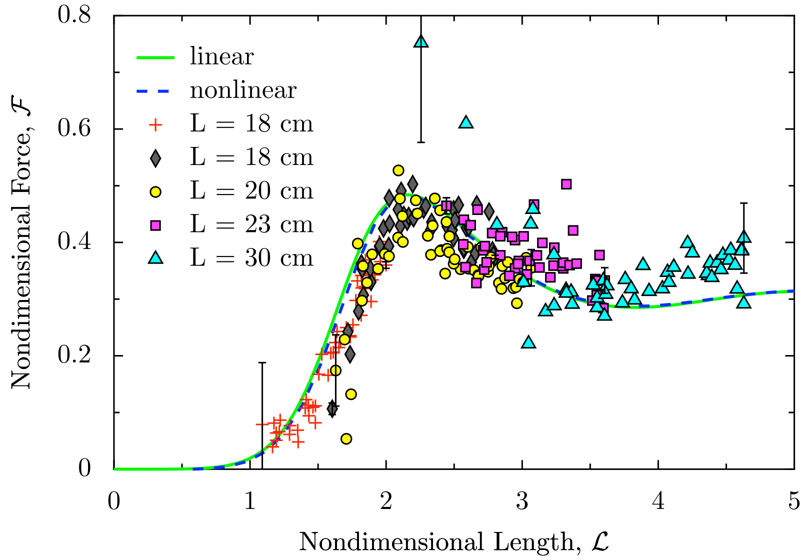

Figure 4-1: Force measurements for various tail lengths, L. Oscillation frequency was varied to span range of dimensionless length, $\mathcal{L}$. + has $D = 0.61\,\mathrm{mm}$ and $a_0 = 0.814\,\mathrm{rad}$. All other data have $D = 0.5\,\mathrm{mm}$ and $a_0 = 0.435\,\mathrm{rad}$.

mary sources of error: thermal drift in the experiment, wall effects, and the neglected nonlinearities in the theory. The error bars in Fig. 4-1 arise from uncertainty in the no-load voltage of the strain gage measurements. At lower oscillation frequencies, the sample time of the experiment increased, leading to noticeable thermal drift in strain gage (force) measurements and thus, larger drift error for the left-most points of a given data-set.

Recall that the wall-correction to the drag coefficients only accounts for a single side-wall of the tank, not the back wall, as is appropriate for all but the longest tails in our experiments. The tip of the longest tail (30 cm, ▲) was only a few centimeters from the back wall and thus, this wall had a non-negligible effect on the drag of the longest tail resulting in an increased thrust as expected. For this tail, it seems logical to use drag coefficients corrected for the effects of this dominant wall. However, the orientation of the tail with respect to the back wall would produce coefficients that vary along the length of the tail; we choose to avoid this complication in our analysis. It is interesting to note that, in these experiments, nonlinear effects are completely negligible relative to the other two sources of error even for long tails and large actuation angles.

This analysis of the propulsive force would not be complete without a comparison to biological micro-swimmers. For this comparison, we take a typical tail length $L = 60\,\mu$m and oscillation frequency $\omega = 135\,$rad/s for bull sperm [4]. For a slender rod in water, we find a drag difference of $\xi_\perp - \xi_\parallel \approx 1 \times 10^{-3}\,$Pa $\cdot$ s. If we assume an optimized swimmer, we have $\mathcal{F} = 0.48$ and $\mathcal{L} = 2.14$ such that $\ell_\omega = L/\mathcal{L} = 28\,\mu$m and take a reasonable amplitude of $a_0 = 0.8\,$rad, we find that Eq. (2.20) gives $F = 67\,$pN. For comparison, bull sperm have measured propulsive forces of $\sim 250\,$pN [29]. This discrepancy in force arises from the fact that RoboChlam is a passive-tail swimmer with torque generated at the base, while sperm is an active-tail swimmer, producing torque along the length of its tail.

4.2 Tail Shapes

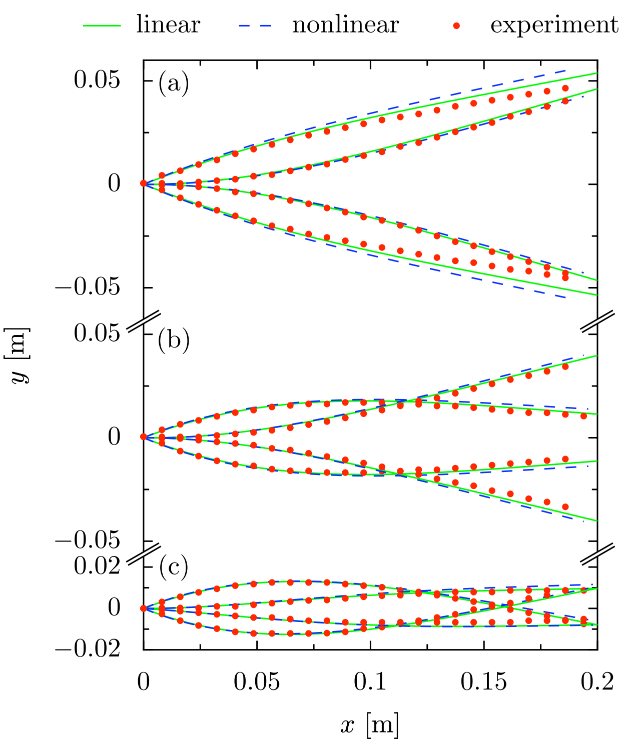

Figure 4-2: Comparison of three tail shapes for a tail with $L = 20\,$cm, $D = 0.5\,$mm, $a_0 = 0.435\,$rad, and oscillation frequencies (a) $\omega = 0.50\,$rad/s ($\mathcal{L} = 1.73$), (b) $\omega = 1.31\,$rad/s ($\mathcal{L} = 2.20$), (c) $\omega = 5.24\,$rad/s ($\mathcal{L} = 3.11$).

In Fig. 4-2, we plot the tail shapes from experiments along with simulations from both the linear and nonlinear theories. The plot shows three tails from a single data set (constant L, D, and a_0, but varying ω) with dimensionless lengths (a) $\mathcal{L} = 1.73$, (b) $\mathcal{L} = 2.20$, and (c) $\mathcal{L} = 3.11$. These dimensionless lengths span the region near the maximum dimensionless force. The tail shapes from experiment matched well with those from the linear and nonlinear simulations, and only slight differences between the three tails were observed. Tails whose dimensionless length was small (Fig. 4-2a) moved stiffly, while those with large dimensionless lengths (Fig. 4-2c) were flexible, as predicted by theory. The difference between the different tail shapes (theory, experiments, simulations) is quantified in Fig. 4-3. The measured errors are observed to be small. The fact that the data match the linear simulation better than the nonlinear solution is fortuitous and merely reflects the fact that resistive force theory is only an approximation of the full hydrodynamic equations [20].

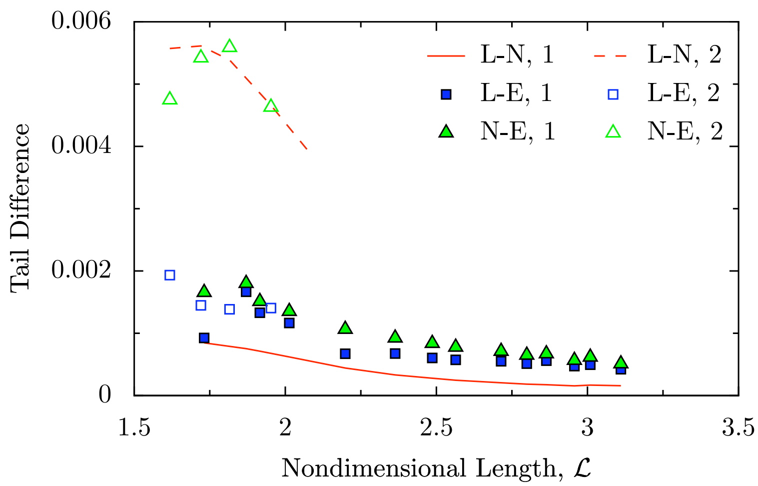

Figure 4-3: Normalized, time-averaged difference between linear (L), nonlinear (N), and experimental (E) tail shapes. The difference is calculated using Eq. (3.13). Two data sets are shown: (1) $L = 20\,\mathrm{cm}$, $D = 0.5\,\mathrm{mm}$, and $a_0 = 0.435\,\mathrm{rad}$; (2) $L = 18\,\mathrm{cm}$, $D = 0.63\,\mathrm{mm}$, and $a_0 = 0.814\,\mathrm{rad}$.

Chapter 5

Conclusions

In summary, we have presented an experimental investigation of Purcell's "flexible oar" propulsive design. Measurements of propulsive forces and time-varying shapes are in agreement with the results of resistive-force theory. Remarkably, the small-slope model of Wiggins & Goldstein [36] appears to remain quantitatively correct well beyond its regime of strict validity.

Although this swimmer compared unfavorably to bull sperm (see §4.1), it is a simpler swimmer to fabricate since it has a single actuation point at the base of the tail compared to the numerous molecular motors along the length of a sperm's tail. Also, the use of multiple tails, a strategy used by *E. coli*, could compensate for the lower propulsive force.

Future Work

A major limitation of this analysis is that the base of the tail is fixed in position. Our future work will investigate the efficiency of this propulsive mechanism when embedded in a synthetic free-swimmer—that is, an elastic filament attached to a body which translates and rotates with the forces and torque generated by the propulsive tail. Preliminary experiments with the free swimmer shown in Fig. 5-1 reveal that rotation of the swimmer body significantly changes the shapes of the tail, modifying the force curve shown in Fig. 4-1, and appreciably impacting the dynamics of the swimmer. It is interesting to note that the large torque and transverse force generated by the tail drag can be cancelled if we have two tails moving antisymmetrically, much like the breast-stroke motion of *Chlamydomonas*.

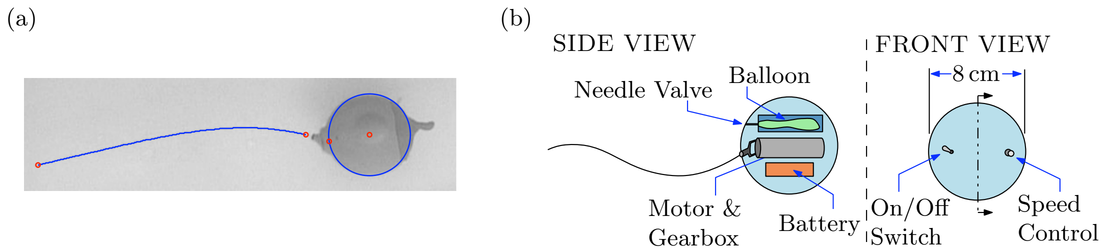

Figure 5-1: Free-swimming RoboChlam. (a) Photograph of swimmer overlayed with the tail-shape and body position extracted from the image. (b) Schematic showing how the original RoboChlam has been encased in foam with a battery and simple controls.

As a final note and a suggestion for future work, the analysis presented herein assumes a Newtonian fluid and a tail with a constant cross-section and uniform material properties. Microorganisms in the body often swim in fluids that are non-Newtonian and thus, it would be interesting to understand the effect of viscoelastic fluids on the motion and propulsive force of an elastic tail. If we remove the second assumption and allow for the cross-section to vary along the tail, the possible waveforms would not be limited by the nondimensional length given in this thesis and this change could produce a more effective swimmer.

Appendix A

Additional Figures and Tables

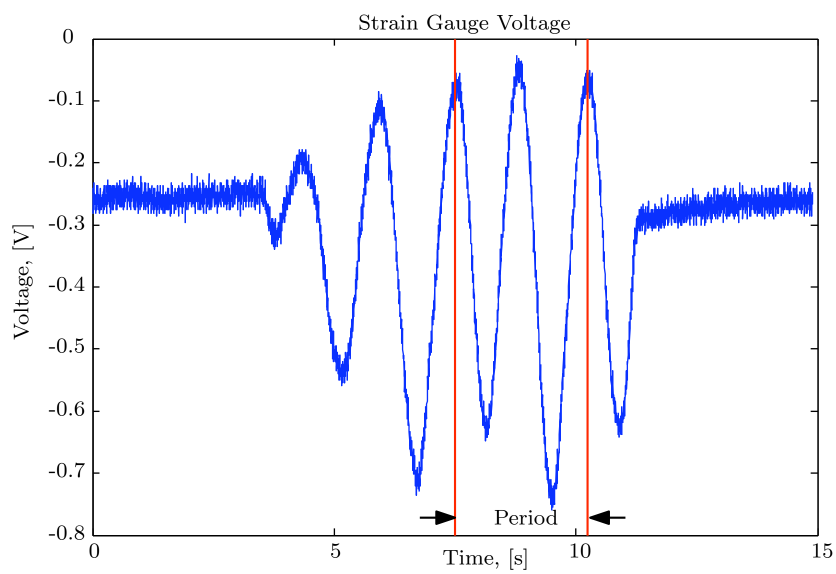

Figure A-1: Strain gage voltage curve proportional to the force generated by oscillatory tail motion. A period of motion has been isolated with an oscillation period of 2.74 s. Note that this period contains two propulsive strokes (negative voltage peaks) and two recovery strokes (positive voltage peaks) because of symmetry in the swimming motion. A slight asymmetry in the two stokes is evident; this was likely caused by imperfections in the Scotch yoke mechanism and skewed placement in the tank leading to asymmetric wall effects. There is also a noticeable difference between the DC voltages before and after swimming; this is likely due to viscoelastic effects in the beam and thermal drift in the circuitry.

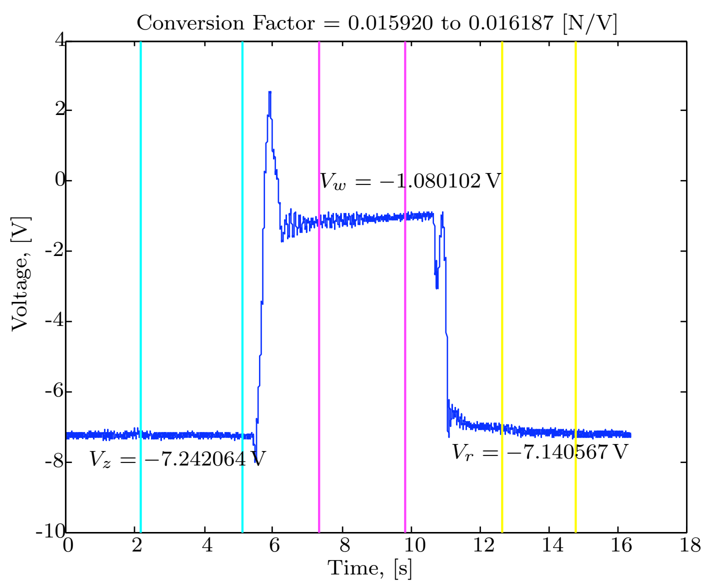

Figure A-2: Sample force calibration measurement using 10 gram weight at the end of the cantilever beam. Colored lines mark the range of data used to measure the voltage of three regions: (1) the initial zero load region with average voltage V_z, (2) during weight application with voltage V_w, and (3) after weight release with voltage V_r. Note the slight DC-voltage increase in region 2 and the slight decrease in region 3; these are likely caused by viscoelastic effects in the beam, but are negligibly small.

Term	Finite Difference	$\frac{\partial f}{\partial \psi_n}$	$\frac{\partial f}{\partial \phi_n}$	$\frac{\partial f}{\partial \tau_n}$	$\frac{\partial f}{\partial \psi}$	$\frac{\partial f}{\partial \phi}$	$\frac{\partial f}{\partial \tau}$	$\frac{\partial f}{\partial \psi_p}$	$\frac{\partial f}{\partial \phi_p}$	$\frac{\partial f}{\partial \tau_p}$
ψ_t	$\frac{\psi-\psi^0}{dt}$				$\frac{1}{dt}$					
$\frac{A}{\xi_\perp}\psi_{ssss}$	$\frac{A}{\xi_\perp}\frac{\phi_p-2\phi+\phi_n}{ds^2}$		$\frac{A}{\xi_\perp ds^2}$			$\frac{-2A}{\xi_\perp ds^2}$			$\frac{A}{\xi_\perp ds^2}$	
$-\frac{1}{\xi_\perp}\tau\psi_{ss}$	$-\frac{1}{\xi_\perp}\tau\phi$					$-\frac{1}{\xi_\perp}\tau$	$-\frac{1}{\xi_\perp}\phi$			
$-B\tau_s\psi_s$	$-B\frac{\tau_p-\tau}{ds}\frac{\psi_p-\psi}{ds}$				$\frac{B}{ds}\frac{\tau_p-\tau}{ds}$		$\frac{B}{ds}\frac{\psi_p-\psi}{ds}$	$-\frac{B}{ds}\frac{\tau_p-\tau}{ds}$		$-\frac{B}{ds}\frac{\psi_p-\psi}{ds}$
$-\frac{A}{\xi_\parallel}\psi_s^2\psi_{ss}$	$-\frac{A}{\xi_\parallel}\left(\frac{\psi_p-\psi}{ds}\right)^2\phi$				$\frac{2A\phi}{\xi_\parallel ds}\frac{\psi_p-\psi}{ds}$	$-\frac{A}{\xi_\parallel}\left(\frac{\psi_p-\psi}{ds}\right)^2$		$\frac{-2A\phi}{\xi_\parallel ds}\frac{\psi_p-\psi}{ds}$		
$\phi-\psi_{ss}$	$\phi-\frac{\psi_p-2\psi+\psi_n}{ds^2}$	$\frac{-1}{ds^2}$			$\frac{2}{ds^2}$	1		$\frac{-1}{ds^2}$		
τ_{ss}	$\frac{\tau_p-2\tau+\tau_n}{ds^2}$			$\frac{1}{ds^2}$			$\frac{-2}{ds^2}$			$\frac{1}{ds^2}$
$A\psi_{ss}^2$	$A\phi^2$					$2A\phi$				
$C\psi_s\psi_{sss}$	$C\frac{\psi_p-\psi}{ds}\frac{\phi_p-\phi}{ds}$				$-\frac{C}{ds}\frac{\phi_p-\phi}{ds}$	$-\frac{C}{ds}\frac{\psi_p-\psi}{ds}$		$\frac{C}{ds}\frac{\phi_p-\phi}{ds}$	$\frac{C}{ds}\frac{\psi_p-\psi}{ds}$	
$-\beta\tau\psi_s^2$	$-\beta\tau\left(\frac{\psi_p-\psi}{ds}\right)^2$				$\frac{2\beta\tau}{ds}\frac{\psi_p-\psi}{ds}$		$-\beta\left(\frac{\psi_p-\psi}{ds}\right)^2$	$\frac{-2\beta\tau}{ds}\frac{\psi_p-\psi}{ds}$		

Table A.1: Finite differences and their derivatives where $\beta = \frac{\xi_\parallel}{\xi_\perp}$, $B = \frac{1}{\xi_\perp} + \frac{1}{\xi_\parallel}$, and $C = A(1+\beta)$. For ψ, δ, and τ, subscripts n and p denote $i-1$ and $i+1$, respectively (no subscript denotes i).

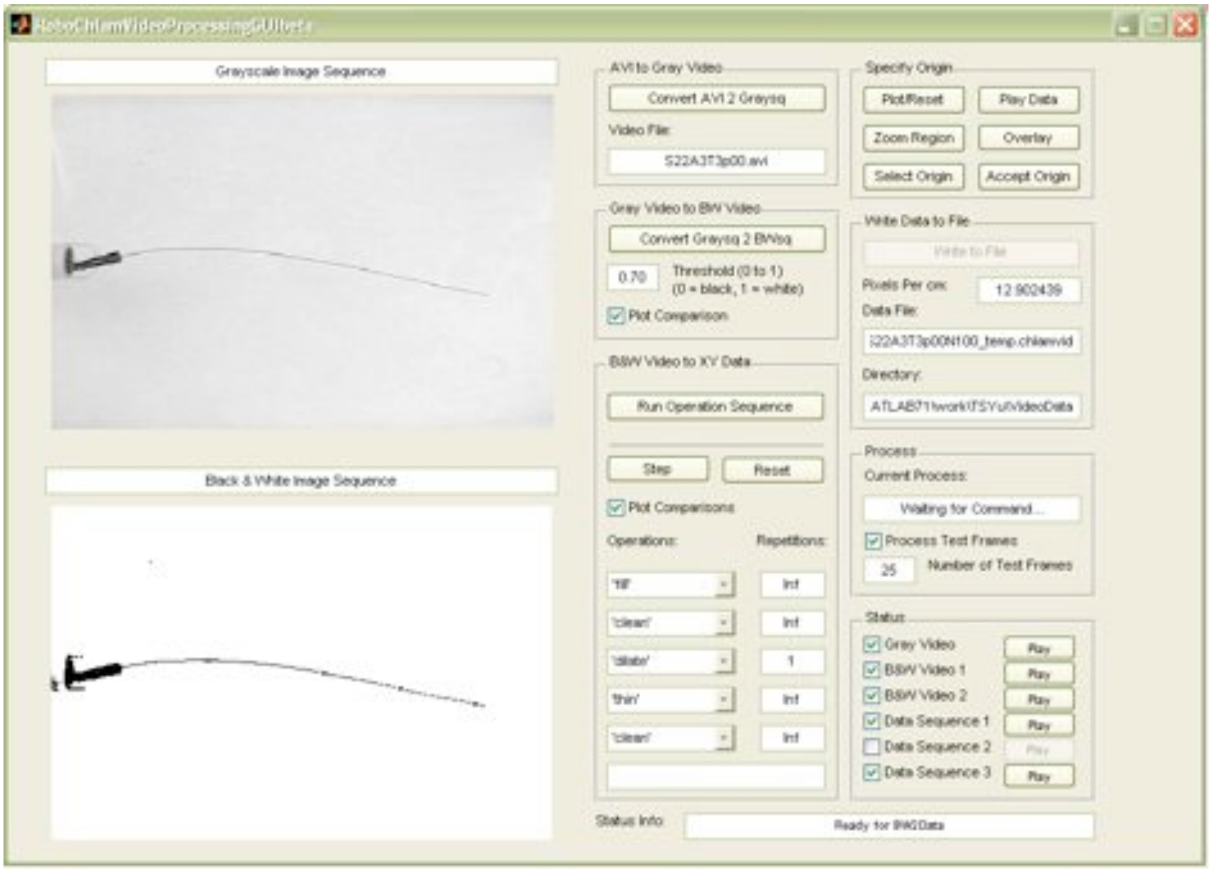

Figure A-3: Screenshot of user interface for video processing.

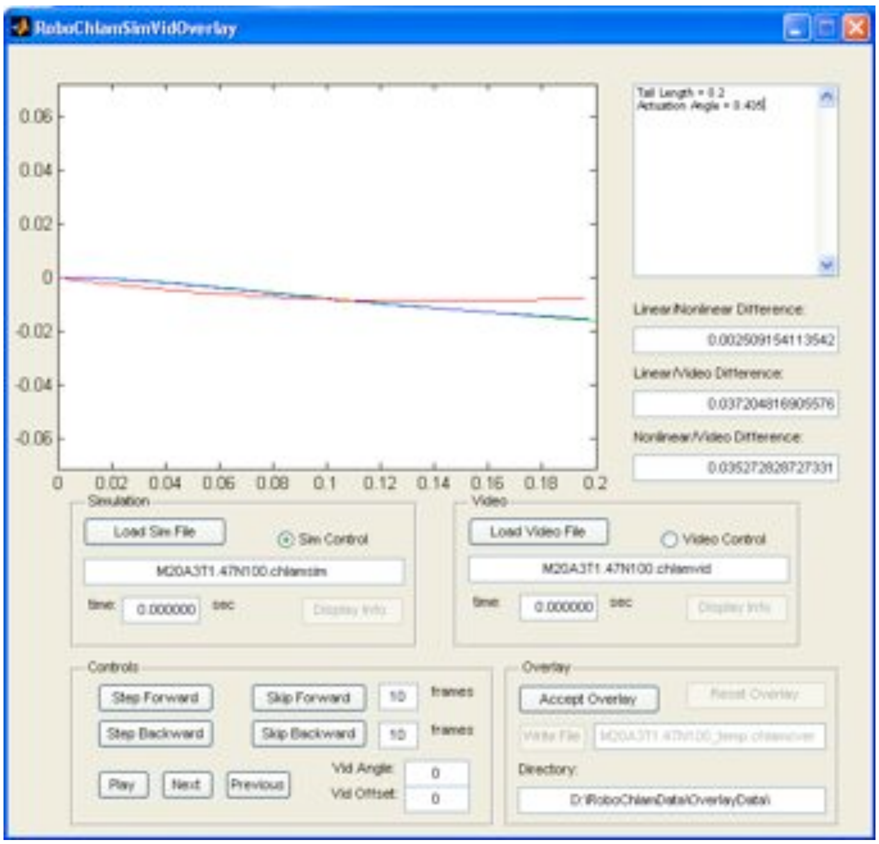

Figure A-4: Screenshot of user interface for comparing experimental and theoretical tail-shapes.

Appendix B

Solution of Governing Equations

Derivations in §B.1 and §B.2 are similar to those found in Camalet and Jülicher [5].

B.1 Elastic Force of Slender Rod

The elastic energy of the tail is given by Eq. (2.7) as

$$\mathcal{E} = \int_0^L \left[\frac{A}{2}\kappa^2 + \frac{\Lambda}{2}{\mathbf{r}_s}^2 \right] ds.$$

The elastic force per unit length is $\mathbf{f}_\epsilon = -\delta\mathcal{E}/\delta\mathbf{r}$, where $\delta/\delta\mathbf{r}$ is the first variation, or functional derivative, with respect to the tail shape $\mathbf{r}$, which is a *function* of the arclength s (hence, *functional* derivative). Note that the curvature of the tail κ is a function of the tail shape. Thus we take

$$\frac{\delta\mathcal{E}}{\delta\mathbf{r}} = \int_0^L \delta \left[\frac{A}{2}\kappa^2 + \frac{\Lambda}{2}{\mathbf{r}_s}^2 \right] ds = \int_0^L \left[A\kappa\delta\kappa + \Lambda\mathbf{r}_s \cdot \delta\mathbf{r}_s \right] ds.$$

The Frenet-Serret equations give

$$\mathbf{r}_s = \hat{\mathbf{t}}, \tag{B.1a}$$

$$\hat{\mathbf{t}}_s = \kappa\hat{\mathbf{n}} = \mathbf{r}_{ss}, \tag{B.1b}$$

$$\hat{\mathbf{n}}_s = -\kappa\hat{\mathbf{t}}, \tag{B.1c}$$

where subscripts denote derivatives. It follows that[1]

$$\begin{aligned}\delta\kappa &= \delta(\hat{\mathbf{n}} \cdot \mathbf{r}_{ss}) \\ &= \hat{\mathbf{n}} \cdot \delta\mathbf{r}_{ss} + \mathbf{r}_{ss}\delta\hat{\mathbf{n}} \\ &= \hat{\mathbf{n}} \cdot \delta\mathbf{r}_{ss}.\end{aligned} \tag{B.2}$$

Now we substitute Eqs (B.1a) and (B.2) into the Eq. (B.1) to give

$$\frac{\delta\mathcal{E}}{\delta\mathbf{r}} = \int_0^L \left[A\kappa\hat{\mathbf{n}} \cdot \delta\mathbf{r}_{ss} + \Lambda\hat{\mathbf{t}} \cdot \delta\mathbf{r}_s\right] ds. \tag{B.3}$$

The goal is to make the integrand in Eq. (B.3) a function of the variation of $\mathbf{r}$ and *not* its derivatives, $\mathbf{r}_s$ or $\mathbf{r}_{ss}$. First we integrate the first term in the integrand by parts[2]

$$\int_0^L [A\kappa\hat{\mathbf{n}} \cdot \delta\mathbf{r}_{ss}]ds = [A\kappa\hat{\mathbf{n}} \cdot \delta\mathbf{r}_s]_0^L - \int_0^L [A\kappa_s\hat{\mathbf{n}} + A\kappa(-\kappa\hat{\mathbf{t}})] \cdot \delta\mathbf{r}_s ds.$$

Further integration by parts[3] gives

$$\begin{aligned}\int_0^L [A\kappa_s\hat{\mathbf{n}} - A\kappa^2\hat{\mathbf{t}})] \cdot \delta\mathbf{r}_s ds = &\left[[A\kappa_s\hat{\mathbf{n}} - A\kappa^2\hat{\mathbf{t}}]\cdot\delta\mathbf{r}\right]_0^L \\ &- \int_0^L \partial_s[A\kappa_s\hat{\mathbf{n}} - A\kappa^2\hat{\mathbf{t}}] \cdot \delta\mathbf{r}\; ds.\end{aligned} \tag{B.4}$$

The first term in the integrand has now been transformed into an integral with $\delta\mathbf{r}$ in the integrand, plus four boundary terms. For the second term in the integrand of Eq. (B.3), we integrate to find[4]:

$$\int_0^L \Lambda\hat{\mathbf{t}} \cdot \delta\mathbf{r}_s ds = \left[\Lambda\hat{\mathbf{t}} \cdot \delta\mathbf{r}\right]_0^L - \int_0^L \partial_s[\Lambda\hat{\mathbf{t}}] \cdot \delta\mathbf{r}\; ds. \tag{B.5}$$

The sum of the integrands on the right-hand sides of Eqs (B.4) and (B.5) is the elastic

---

[1] Here we have used: $\mathbf{r}_{ss} = \hat{\mathbf{t}}_s = \kappa \cdot \hat{\mathbf{n}}$ so that $\mathbf{r}_{ss}\delta\hat{\mathbf{n}} = \kappa\hat{\mathbf{n}} \cdot \delta\hat{\mathbf{n}} = 0$ ($\hat{\mathbf{n}}$ and $\delta\hat{\mathbf{n}}$ are orthogonal).

[2] We let $u = A\kappa\hat{\mathbf{n}}$ and $dv = \delta\mathbf{r}_{ss}ds$.

[3] $u = [A\kappa_s\hat{\mathbf{n}} - A\kappa^2\hat{\mathbf{t}}]$ and $dv = \delta\mathbf{r}_s ds$

[4] $u = \Lambda\hat{\mathbf{t}}$ and $dv = \delta\mathbf{r}_s ds$.

force[5]:

$$\mathbf{f}_\epsilon = -\frac{\delta \mathcal{E}}{\delta \mathbf{r}} = -\partial_s[A\kappa_s \hat{\mathbf{n}} - A\kappa^2 \hat{\mathbf{t}} + \Lambda \hat{\mathbf{t}}]. \tag{B.6}$$

The force in the tangential direction can be defined as the tension so that Eq. (B.6) gives, $\Lambda = -\tau + A\kappa^2$ [5], and we have

$$\begin{aligned}
\mathbf{f}_\epsilon &= -\partial_s[A\kappa_s \hat{\mathbf{n}} - \tau \hat{\mathbf{t}}] \\
&= -A\kappa_{ss}\hat{\mathbf{n}} + A\kappa_s\kappa\hat{\mathbf{t}} + \kappa\tau\hat{\mathbf{n}} + \tau_s\hat{\mathbf{t}} \\
&= -(A\kappa_{ss} - \kappa\tau)\hat{\mathbf{n}} + (A\kappa_s\kappa + \tau_s)\hat{\mathbf{t}}
\end{aligned} \tag{B.7}$$

B.2 Nonlinear Equations of Motion

To solve for the equations of motion, recall Eq. (2.6) from resistive-force theory

$$\mathbf{f}_d = -[\xi_\perp \hat{\mathbf{n}}\hat{\mathbf{n}} + \xi_\| \hat{\mathbf{t}}\hat{\mathbf{t}}] \cdot \mathbf{r}_t.$$

Since each segment of the tail is in equilibrium, the local drag force must be balanced by the local elastic force, such that $\mathbf{f}_d + \mathbf{f}_\epsilon = 0$. Now substitute the drag force, $\mathbf{f}_d$, and dot both sides by $[(1/\xi_\perp)\hat{\mathbf{n}}\hat{\mathbf{n}} + (1/\xi_\|)\hat{\mathbf{t}}\hat{\mathbf{t}}]$ to find

$$r_t = \left(\frac{1}{\xi_\perp}\hat{\mathbf{n}}\hat{\mathbf{n}} + \frac{1}{\xi_\|}\hat{\mathbf{t}}\hat{\mathbf{t}}\right) \cdot \mathbf{f}_\epsilon. \tag{B.8}$$

If we substitute the elastic force, $\mathbf{f}_\epsilon$ into the equation above, we get

$$\begin{aligned}
r_t &= \left(\frac{1}{\xi_\perp}\hat{\mathbf{n}}\hat{\mathbf{n}} + \frac{1}{\xi_\|}\hat{\mathbf{t}}\hat{\mathbf{t}}\right) \cdot \left[-(A\kappa_{ss} - \kappa\tau)\hat{\mathbf{n}} + (A\kappa_s\kappa + \tau_s)\hat{\mathbf{t}}\right], \\
&= -\frac{1}{\xi_\perp}(A\psi_{sss} - \psi_s\tau)\hat{\mathbf{n}} + \frac{1}{\xi_\|}(A\psi_{ss}\psi_s + \tau_s)\hat{\mathbf{t}},
\end{aligned} \tag{B.9}$$

where $\kappa = \psi_s$.

From Eqs (B.1a) and (B.1b) it follows that $\partial_t \mathbf{r}_s = \hat{\mathbf{n}}\psi_t$. Thus, the equation of motion for $\psi(s)$ is found by taking the spacial derivative of Eq. (B.9) and keeping

[5] $\delta F = \int \left(\frac{\delta F}{\delta g(x)}\right) \delta g(x) dx.$

only the $\hat{\mathbf{n}}$ component so that

$$\psi_t = -\frac{1}{\xi_\perp}(-\psi_s\tau_s + A\psi_{ssss} - \psi_{ss}\tau) + \frac{1}{\xi_\parallel}(A\psi_{ss}{\psi_s}^2 + \psi_s\tau_s). \tag{B.10}$$

The above equation is the first equation of motion.

The second equation of motion is found by assuming that the elastica is incompressible along its length so that it satisfies the constraint $\partial_t {\mathbf{r}_s}^2 = 2\mathbf{r}_s \cdot \partial_t \mathbf{r}_s = 2\hat{\mathbf{t}} \cdot \partial_t \mathbf{r}_s = 0$. In other words, we take the derivative of Eq. (B.9) w.r.t. s and keep only the $\hat{\mathbf{t}}$ component to find

$$\tau_{ss} - \frac{\xi_\parallel}{\xi_\perp}{\psi_s}^2\tau = -\left(1 + \frac{\xi_\parallel}{\xi_\perp}\right) A\psi_{sss}\psi_s - A{\psi_{ss}}^2. \tag{B.11}$$

In order to solve these nonlinear equations numerically, we rewrite Eqs (B.10) and (B.11) as a system of second order partial differential equations:

$$f_1 = \psi_t + \frac{1}{\xi_\perp}\left(A\phi_{ss} - \tau\phi - \tau_s\psi_s\right) - \frac{1}{\xi_\parallel}\left(A{\psi_s}^2\phi + \tau_s\psi_s\right) = 0, \tag{B.12a}$$

$$f_2 = \phi - \psi_{ss} = 0, \tag{B.12b}$$

$$f_3 = \tau_{ss} - \beta\tau{\psi_s}^2 + A\left(1 + \frac{\xi_\parallel}{\xi_\perp}\right)(\psi_s\phi_s) + A\phi^2 = 0. \tag{B.12c}$$

B.3 Linear Equations of Motion

We will start with Eqs (B.6) and (B.8):

$$r_t = -\left(\frac{1}{\xi_\perp}\hat{\mathbf{n}}\hat{\mathbf{n}} + \frac{1}{\xi_\parallel}\hat{\mathbf{t}}\hat{\mathbf{t}}\right)\cdot \mathbf{f}_\epsilon,$$

$$\mathbf{f}_\epsilon = -\partial_s[A\kappa_s\hat{\mathbf{n}} - A\kappa^2\hat{\mathbf{t}}] = (-A\kappa_{ss} + A\kappa^3)\hat{\mathbf{n}} + 3A\kappa\kappa_s\hat{\mathbf{t}}. \tag{B.13}$$

Notice that the inextensibility constraint, Λ, does not appear in the elastic force above because inextensibility is implied for small deformations. Combining these two equations, we get:

$$
\begin{aligned}
r_t =& \left(\frac{1}{\xi_\perp} \hat{\mathbf{n}}\hat{\mathbf{n}} + \frac{1}{\xi_\parallel} \hat{\mathbf{t}}\hat{\mathbf{t}} \right) \cdot (-A\kappa_{ss} + A\kappa^3)\hat{\mathbf{n}} + 3A\kappa\kappa_s \hat{\mathbf{t}} \\
=& - \frac{1}{\xi_\perp}(A\kappa_{ss} - A\kappa^3)\hat{\mathbf{n}} + \frac{1}{\xi_\parallel} 3A\kappa\kappa_s \hat{\mathbf{t}}.
\end{aligned} \tag{B.14}
$$

From geometry, we know that

$$
\kappa = \frac{d\psi}{ds} = \frac{y_{xx}}{\sqrt{1+y_x^2}} \approx y_{xx}, \tag{B.15a}
$$

$$
\hat{\mathbf{n}} = \frac{1}{\sqrt{1+y_x^2}} \begin{bmatrix} -y_x \\ 1 \end{bmatrix} \approx \begin{bmatrix} -y_x \\ 1 \end{bmatrix}, \tag{B.15b}
$$

$$
\hat{\mathbf{t}} = \frac{1}{\sqrt{1+y_x^2}} \begin{bmatrix} 1 \\ y_x \end{bmatrix} \approx \begin{bmatrix} 1 \\ y_x \end{bmatrix}. \tag{B.15c}
$$

The final step in the above equations assumes that the tail is undergoing small deformation and thus $y_x \ll 1$. We can now rescale our equations, such that $y = h\tilde{y}$ and $x = L\tilde{x}$, where $h/L = \epsilon$ and split the velocity into components so that $r_t = (x_t, y_t)$. Thus,

$$
\begin{aligned}
\tilde{x}_t =& \frac{1}{\xi_\perp} \left(A\frac{h}{L^4}\tilde{y}_{\tilde{x}\tilde{x}\tilde{x}\tilde{x}} - A\frac{h^3}{L^6}\tilde{y}^3_{\tilde{x}\tilde{x}} \right) \frac{h}{L}\tilde{y}_{\tilde{x}} + \frac{1}{\xi_\parallel} 3A\frac{h^2}{L^5}\tilde{y}_{\tilde{x}\tilde{x}}\tilde{y}_{\tilde{x}\tilde{x}\tilde{x}} \\
=& \frac{1}{\xi_\perp} \left(A\frac{\epsilon^2}{L^3}\tilde{y}_{\tilde{x}\tilde{x}\tilde{x}\tilde{x}}\tilde{y}_{\tilde{x}} - A\frac{\epsilon^4}{L^4}\tilde{y}^3_{\tilde{x}\tilde{x}}\tilde{y}_x \right) + \frac{1}{\xi_\parallel} 3A\frac{\epsilon^2}{L^3}\tilde{y}_{\tilde{x}\tilde{x}}\tilde{y}_{\tilde{x}\tilde{x}\tilde{x}},
\end{aligned}
$$

and

$$
\begin{aligned}
\tilde{y}_t =& - \frac{1}{\xi_\perp} \left(A\frac{h}{L^4}\tilde{y}_{\tilde{x}\tilde{x}\tilde{x}\tilde{x}} - A\frac{h^3}{L^6}\tilde{y}^3_{\tilde{x}\tilde{x}} \right) - \frac{1}{\xi_\parallel} 3A\frac{h^2}{L^5}\tilde{y}_{\tilde{x}\tilde{x}}\tilde{y}_{\tilde{x}\tilde{x}\tilde{x}}\frac{h}{L}\tilde{y}_x \\
=& - \frac{1}{\xi_\perp} \left(A\frac{\epsilon}{L^3}\tilde{y}_{\tilde{x}\tilde{x}\tilde{x}\tilde{x}} - A\frac{\epsilon^3}{L^3}\tilde{y}^3_{\tilde{x}\tilde{x}} \right) - \frac{1}{\xi_\parallel} 3A\frac{\epsilon^3}{L^3}\tilde{y}_{\tilde{x}}\tilde{y}_{\tilde{x}\tilde{x}}\tilde{y}_{\tilde{x}\tilde{x}\tilde{x}}.
\end{aligned}
$$

where derivatives in s have become derivatives in x for small slopes. Eliminating orders of ϵ greater than unity, we find that our linearized equations of motion are:

$$\begin{aligned} x_t &= 0, \\ y_t &= -\frac{1}{\xi_\perp} A y_{xxxx}. \end{aligned} \tag{B.16}$$

B.4 Linear Propulsive Force

The definition of the time average propulsive force is given by Eq. (2.16):

$$\langle F \rangle \equiv -\frac{1}{T} \int_0^T \int_0^L \mathbf{f} \cdot \hat{\mathbf{e}}_x \, ds \, dt, \tag{B.17}$$

where T is the period of oscillation. The negative sign on the right-hand side of the above equation appears because the propulsive direction is negative (see Fig. 2-3). The hydrodynamic drag force given by Eq. (2.6) is:

$$\mathbf{f}_d = [\xi_\perp \hat{\mathbf{n}}\hat{\mathbf{n}} + \xi_\parallel \hat{\mathbf{t}}\hat{\mathbf{t}}] \cdot \mathbf{r}_t,$$

where the free stream velocity $\mathbf{u} = 0$. The local slope of the elastica is given by $\psi(s)$, such that the local unit normal and unit tangent can be expressed as

$$\hat{\mathbf{n}} = \begin{bmatrix} \sin\psi \\ -\cos\psi \end{bmatrix}, \qquad \hat{\mathbf{t}} = \begin{bmatrix} \cos\psi \\ \sin\psi \end{bmatrix}. \tag{B.18}$$

The tensor products of these unit vectors become

$$\hat{\mathbf{n}}\hat{\mathbf{n}} = \begin{bmatrix} \sin^2\psi & -\sin\psi\cos\psi \\ -\sin\psi\cos\psi & \cos^2\psi \end{bmatrix}, \qquad \hat{\mathbf{t}}\hat{\mathbf{t}} = \begin{bmatrix} \cos^2\psi & \sin\psi\cos\psi \\ \sin\psi\cos\psi & \sin^2\psi \end{bmatrix}. \tag{B.19}$$

For small angles we can approximate $\sin\psi$ and $\cos\psi$ as

$$\sin\psi \approx y_x, \qquad \cos\psi \approx 1 \tag{B.20}$$

and we can let

$$\mathbf{r}_t = \begin{bmatrix} x_t \\ y_t \end{bmatrix} \approx \begin{bmatrix} 0 \\ y_t \end{bmatrix}, \tag{B.21}$$

recalling that subscripts denote derivatives. Since we are only concerned with the x-component of the force, we can take the x-component of Eq. (B.19) and also substitute Eqs (B.20) and (B.21) to give

$$f_x = \left(\xi_\perp \begin{bmatrix} {y_x}^2 \\ -y_x \end{bmatrix} + \xi_\parallel \begin{bmatrix} 1 \\ y_x \end{bmatrix} \right) \cdot \begin{bmatrix} 0 \\ y_t \end{bmatrix} \tag{B.22}$$

$$= (\xi_\parallel - \xi_\perp) y_x y_t. \tag{B.23}$$

Note that the subscript of f_x describes the x-component of local drag force and is not a derivative. Pausing a moment to analyze the above equation, we see that the local propulsive force is simply a product of the drag difference, the local slope, and the vertical velocity. The above equation is exactly where physical arguments should lead: for a nearly horizontal rod moving in the vertical direction, the transverse drag would be large, but only a small component of the transverse drag ($y_x \xi_\perp$) would act in the x-direction. Similarly, a small component of the velocity ($y_x y_t$) is along the axial direction.

If we substitute Eq. (2.11) into the equation above we get

$$f_x = A \frac{\xi_\perp - \xi_\parallel}{\xi_\perp} y_x y_{xxxx} = A \frac{\xi_\perp - \xi_\parallel}{\xi_\perp} \left[\frac{d}{dx}(y_x y_{xxx}) - (y_{xx} y_{xxx}) \right] \tag{B.24}$$

$$= A \frac{\xi_\perp - \xi_\parallel}{\xi_\perp} \left[\frac{d}{dx}(y_x y_{xxx}) - \frac{d}{dx} \left(\frac{1}{2} y_{xx}^2 \right) \right]. \tag{B.25}$$

Thus the propulsive force is

$$F = \int_0^L A \frac{\xi_\perp - \xi_\parallel}{\xi_\perp} \left[\frac{d}{dx}(y_x y_{xxx}) - \frac{d}{dx} \left(\frac{1}{2} y_{xx}^2 \right) \right] dx$$

$$= A \frac{\xi_\perp - \xi_\parallel}{\xi_\perp} \left[y_x y_{xxx} - \frac{1}{2} y_{xx}^2 \right]_{x=0}, \tag{B.26}$$

recalling that $y_{xx} = y_{xxx} = 0$ at $x = L$ as shown in Tbl. 2.2. Now we can substitute this expression into Eq. (B.17)

$$\langle F \rangle = -A \frac{\xi_\perp - \xi_\parallel}{\xi_\perp} \frac{1}{T} \int_0^T \left[y_x y_{xxx} - \frac{1}{2} y_{xx}^2 \right]_{x=0} dt. \tag{B.27}$$

Bibliography

[1] L.E. Becker, S.A. Koehler, and H.A. Stone. On self-propulsion of micro-machines at low reynolds number: Purcell's three-link swimmer. *Journal of Fluid Mechanics*, 490:15–35, 2003.

[2] H. C. Berg. *E. coli in Motion*. Springer-Verlag, NY, 2004.

[3] D. Bray. *Cell Movements*. Garland Publishing, New York, NY, 2000.

[4] C. Brennen and H. Winet. Fluid mechanics of propulsion by cilia and flagella. *Annual Review of Fluid Mechanics*, 9:339–398, 1977.

[5] S. Camalet and F. Julicher. Generic aspects of axonemal beating. *New Journal of Physics*, 2:1–23, 2000.

[6] Brian Chan. Propulsion devices for locomotion at low reynolds number. Master's thesis, Massachusetts Institute of Technology, 2004.

[7] S. Childress. *Mechanics of Swimming and Flying*. Cambridge Studies in Mathematical Biology. Cambridge University Press, Cambridge, 1st edition, 1981.

[8] R G Cox and S G Mason. Suspended Particles in Fluid Flow Through Tubes. *Annual Review of Fluid Mechanics*, 3(1):291–316, 1971.

[9] Roy R. Craig. *Mechanics of Materials*. John Wiley & Sons, Inc., second edition, 2000.

[10] N. J. De Mestre and W. B. Russel. Low-reynolds-number translation of a slender cylinder near a plane wall. *Journal of Engineering Mathematics*, 9:81–91, 1975.

[11] R. Dreyfus, J. Baudry, M. L. Roper, M. Fermigier, H. A. Stone, and J. Bibette. Microscopic artificial swimmers. *Nature*, 437:862–865, 2005.

[12] Richard S. Figliola and Donald E. Beasley. *Theory and Design for Mechanical Measurements*. John Wiley & Sons, Inc., third edition, 2000.

[13] J. Gray and G. J. Hancock. The propulsion of sea-urchin spermatozoa. *J. Exp. Biol.*, 32:802–814, 1955.

[14] R. W. Hamming. *Numerical Methods for Scientists and Engineers*. Dover Publications, 1973.

[15] M. Kim and T. R. Powers. Hydrodynamic interactions between rotating helices. *Physical Review E*, 69(6):061910, June 2004.

[16] Y. W. Kim and R. R. Netz. Pumping fluids with periodically beating grafted elastic filaments. *Physical Review Letters*, 96:158101, 2006.

[17] S. A. Koehler and T. R. Powers. Twirling Elastica: Kinks, Viscous Drag, and Torsional Stress. *Physical Review Letters*, 85(22):4827–4830, 2000.

[18] M.C. Lagomarsino. *Biologically Inspired Problems Concerning Semiflexible Filaments*. PhD thesis, FOM Institute for Atomic and Molecular Physics (AMOLF), 2004.

[19] Eric Lauga, Willow R. DiLuzio, George M. Whitesides, and Howard A. Stone. Swimming in circles: Motion of bacteria near solid boundaries. *Biophysical Journal*, 90:400, 2005.

[20] J. Lighthill. Flagellar hydrodynamics - The John von Neumann lecture, 1975. *SIAM Review*, 18:161–230, 1976.

[21] James LIghthill. *Mathematical Biofluiddynamics*. SIAM, 1975.

[22] C. P. Lowe. Dynamics of filaments: modelling the dynamics of driven microfilaments. *Philosophical Transactions of the Royal Society of London, Series B-Biological Sciences*, 358:1543–1550, 2003.

[23] K. E. Machin. Wave propagation along flagella. *Journal of Experimental Biology*, 35:796–806, 1958.

[24] K. E. Machin. The control and synchronization of flagellar movement. *Proceedings of the Royal Society, B*, 158:88–104, 1963.

[25] William H. Press, Brian P. Flannery, Saul A. Teukolsky, and William T. Vetterling. *Numerical Recipes in C : The Art of Scientific Computing*. Cambridge University Press, 1992.

[26] E. M. Purcell. Life at low reynolds number. *American Journal of Physics*, 45:3–11, 1977.

[27] E. M. Purcell. The efficiency of propulsion by a rotating flagellum. *Proceedings of the National Academy of Sciences of the United States of America*, 94:11307–11311, 1997.

[28] M. Roper, R. Dreyfus, J. Baudry, M. Fermigier, J. Bibette, and H. A. Stone. On the dynamics of magnetically driven elastic filaments. *Journal of Fluid Mechanics*, 554:167–190, May 2006.

[29] Kathleen A. Schmitz, Dana L. Holcomb-Wygle, Danial J. Oberski, and Charles B. Lindemann. Measurement of the Force Produced by an Intact Bull Sperm Flagellum in Isometric Arrest and Estimation of the Dynein Stall Force. *Biophysical Journal*, 79(1):468–478, 2000.

[30] John F. Stalnaker and R. G. Hussey. Wall effects on cylinder drag at low reynolds number. *Physics of Fluids*, 22:603–613, 1979.

[31] Daniel Tam and A. E. Hosoi. Optimal stroke patterns for purcell's three link swimmer. *Phys. Rev. Lett.*, In Review.

[32] G. I. Taylor. Analysis of the swimming of microscopic organisms. *Proceedings of the Royal Society, A*, 209:447–461, 1951.

[33] G. I. Taylor. The action of waving cylindrical tails in propelling microscopic organisms. *Proceedings of the Royal Society, A*, 211:225–239, 1952.

[34] S. Vogel. *Life in Moving Fluids: The Physical Biology of Flow*. Princeton University Press, 1994.

[35] C. H. Wiggins, D. Riveline, A. Ott, and R. E. Goldstein. Trapping and wiggling: Elastohydrodynamics of driven microfilaments. *Biophysical Journal*, 74:1043–1060, 1998.

[36] Chris H. Wiggins and Raymond E. Goldstein. Flexive and propulsive dynamics of elastica at low reynolds number. *Physical Review Letters*, 80:3879–3882, 1998.

[37] C. W. Wolgemuth, T. R. Powers, and R. E. Goldstein. Twirling and whirling: Viscous dynamics of rotating elastic filaments. *Physical Review Letters*, 84:1623–1626, 2000.